

Context-aware UAV LiDAR reveals forest structure and improves tree diameter estimates in subalpine forest

Jaime C. Revenga^{1,2,3} | Stefan Oehmcke^{4,5} | Mana Gharun⁶ | Flurin Sutter⁷ | Fabian Gieseke^{5,8} | Katerina Trepekli⁹ | Nina Buchmann¹⁰ | Alexander Damm^{11,12}

¹Department of Biology, Section for Ecoinformatics and Biodiversity, Aarhus University, Denmark.

²Center for Landscape Research in Sustainable Agricultural Futures (Land-CRAFT), Aarhus University, Ole Worms Allé 3, 8000 Aarhus, Denmark

³Department of Geosciences and Natural Resources Management, University of Copenhagen, Øster Voldgade 10, 1350 Copenhagen, Denmark.

⁴Institute for Visual and Analytic Computing, University of Rostock, Albert-Einstein-Straße 21, 18059 Rostock, Germany.

⁵Department of Computer Science, University of Copenhagen, Universitetsparken 1, 2100 Copenhagen, Denmark.

⁶Institute of Landscape Ecology, Research Unit for Biosphere-Atmosphere Interaction, University of Münster, Heisenbergstr. 2, 48149 Münster, Germany.

⁷Swiss Federal Institute for Forest, Snow and Landscape Research (WSL), Forest Dynamics Research Unit, Zürcherstrasse 111, 8903 Birmensdorf, Switzerland.

⁸Machine Learning and Data Engineering, Department of Information Systems, University of Münster, Leonardo Campus 3, 48149 Münster, Germany.

⁹Department of Geology and Geoenvironment, National and Kapodistrian University of Athens, University Campus 157 72, Zografou, Athens, Greece.

¹⁰Department of Environmental Systems

1. Forest structure, tree diameter, and aboveground biomass (AGB) are central variables in trait-based ecology and forest management, and recent advances in Unmanned Aerial Vehicle (UAV) and LiDAR surveys have substantially improved tree-level phenotyping of these structural attributes. **2.** Building on these developments, machine learning (ML) applications are increasingly used to refine tree-diameter estimates and, by extension, improve AGB predictions derived from allometric relationships. **3.** Here, we evaluated the capacity of shallow learning methods to leverage local information from the surrounding context of the tree of interest to improve predictions of stem diameter and tree-level AGB, over 33 ha of a Norway spruce forest (Davos, CH). **4.** Our objectives were to (i) characterise gradients of tree height, (ii) examine group-level morphology of tree assemblages as an indicator of forest structural organisation, and (iii) assess whether these patterns can be leveraged to improve tree diameter and AGB predictions. **5.** We segmented the point cloud data scene into individual canopies and focused on LiDAR-derived tree canopy features. We

then used local indicators of spatial association of tree heights to characterise local context and identified tree assemblages within the forest. Assemblage-level metrics were first analysed to characterise forest spatial structure and ecological similarity, and subsequently evaluated as additional predictors in ML regression experiments for tree diameter. The focus was on comparing performance of tree diameter predictions between twin regression methods that either consider assemblage metrics (i.e. context-aware), or not. Then, the improvements provided by context awareness were assessed in terms of accuracy gained in estimating tree diameter and AGB. 6. We obtained results of three different shallow learning methods and evaluated these based on nested cross-validation. We considered two datasets within the same site: one being scattered in sparse measurement plots, the other spatially continuous. 7. In both sparse and continuous datasets, we found enhanced prediction performance in context-aware regressions, where RMSE on tree diameter estimation was reduced by 4.1% and by 0.8%, respectively, suggesting that a heterogeneous context supports enhanced estimates.

8. **Practical implication:** Gradients of tree height can reflect underlying ecological drivers of forest structure, and this structural information may be leveraged to enhance predictions of tree diameter and AGB. The method proposed is fully native to UAV LiDAR data.

KEY WORDS

forest structure, tree diameter, aboveground biomass, environmental monitoring, machine learning, context-aware modeling, LiDAR, UAV

51 1 | INTRODUCTION

52 Natural forests exhibit complex structures shaped by underlying ecological processes such as competition, facilitation,
53 acclimation and disturbance dynamics. These processes influence tree structure and aboveground biomass (AGB),
54 both of which are key variables in forest ecology and management. AGB plays a major role in determining global
55 carbon budgets, and forests are essential for regulating carbon exchange between the atmosphere and the biosphere

(Faticchi et al., 2019; Pörnter et al., 2022). Despite substantial advances in environmental remote sensing, current assessments of forest carbon cycling remain uncertain, with contrasting findings partly attributed to limited accuracy in AGB estimation (Baccini et al., 2017; Friedlingstein et al., 2019; Gundersen et al., 2021). This highlights the need for methods that improve characterization of forest spatial structure and improve accuracy and spatial resolution of forest AGB estimates from remotely sensed data (Duncanson et al., 2019).

Predictive analyses in forest phenotyping and AGB from remote sensing surveys have traditionally been focused on regressions considering only individual tree attributes as predictors (e.g. tree height, canopy metrics) (Yao et al., 2014; Santini et al., 2019) and fitted allometric models (Dalponte and Coomes, 2016). Such tree-level analyses have been crucial for improving the characterization of optical vegetation traits (Kükenbrink et al., 2019), tree dendrometry (Cabo et al., 2018), and species composition (Kukkonen et al., 2019). However, these approaches generally do not account for the influence of spatial context on the individual tree traits under investigation, including both abiotic factors (e.g., terrain conditions, soil depth) and biotic interactions (e.g., light interception, nutrient competition). Moreover, it is well established that local context—encompassing microclimatic, edaphic, and biotic conditions—strongly shapes tree traits, and that individual tree performance is influenced by the combined effects of abiotic stress and biotic interactions (Bertness and Callaway, 1994; Maestre et al., 2009). Furthermore, a line of research has aimed to measure tree performance components (e.g. stature, dominance, wood density) across environmental gradients, while monitoring local biotic interactions (Valladares and Niinemets, 2008; Muscarella et al., 2018). Indeed, an increasing number of empirical studies, have proposed different methods to use the information of neighboring trees to enhance individual tree trait estimates (i.e. metrics derived from monitoring inventory plots), such as non-linear mixed effects methods (Hao et al., 2020; Yang et al., 2020; Liu et al., 2021), or competition-based methods (Lo and Lin, 2012; Sun et al., 2019; Zhang et al., 2020). This line of research has shown that considering neighborhood information can improve trait estimates, and its positive impact has been documented in various tree-level regression analyses, e.g. productivity (Potvin and Dutilleul, 2009; Ratcliffe et al., 2015), fuel potential (Andersen et al., 2005) or structural metrics (Næsset and Økland, 2002; Rijal et al., 2012; Liu et al., 2021).

However, despite the utility of current methods that leverage neighborhood metrics such as tree stand information, from an object-based remote sensing perspective they result suboptimal in some respects. Many of such methods are not directly transferable to a remote sensing framework because they use understory metrics as predictors (e.g. stem diameter of neighboring trees), which are difficult to survey reliably from an above-canopy perspective (Sun et al., 2019; Zhang et al., 2020). Additionally, questions remain about the optimal scale at which such neighborhood metrics become relevant and therefore should be retrieved (Potvin and Dutilleul, 2009; Ratcliffe et al., 2015). A common procedure is to consider the trees contained in an arbitrarily delineated inventory plot, whose size is defined to fit management purposes (Ratcliffe et al., 2015). This approach, although useful for monitoring tasks, can pose the shortcoming of overlooking the spatial scale at which relevant ecological phenomena operate (e.g. the appropriate range at which tree competition effects are significant), so the analysis remains constrained by the effects observed at the scale of the plot size (Sun et al., 2019; Zhang et al., 2020; Hao et al., 2020; Yang et al., 2020; Liu et al., 2021). To the best of our knowledge, tree-level AGB and trait assessments considering neighborhood information are currently limited due to one or more of the following reasons: (i) they characterise the spatial context with uniquely process-specific indices (e.g. competition pressure from immediate neighbors) (Lo and Lin, 2012; Sun et al., 2019; Zhang et al., 2020); (ii) they calibrate models with neighborhood-metrics retrieved from artificially-bounded inventory plots (e.g. nonlinear mixed-effects methods) (Hao et al., 2020; Yang et al., 2020; Liu et al., 2021); or (iii) they overlook the spatial scale at which an ecological phenomenon affects the trait under investigation. Moreover, when the relationship between the plot-level predictors used and any ecological phenomenon is described, often ancillary data sources are incorporated (e.g. tree stand age) (Antonio et al., 2007; Zhang et al., 2020) or less strictly quantified forest management metrics,

99 e.g. "stand quality", "site index", "dominance index" (Antonio et al., 2007; Yang et al., 2020; Zhang et al., 2020). These
100 shortcomings are constrained by the specific data collection protocol, and currently hinder transferring such methods
101 to an integrated remote sensing framework, which would offer greater flexibility for conducting standardized, scalable,
102 and replicable forest analyses.

103 Unstaffed Aerial Vehicles (UAV) equipped with Light Detection and Ranging (LiDAR) monitoring systems are re-
104 garded as particularly versatile (Hyppä et al., 2020), accurate and cost-effective tools (Li et al., 2022) to contribute
105 to the task of extensive phenotyping, bridging scales in AGB mapping, particularly covering the scale between *in*
106 *situ* field-based inventories (approx. 0-1 ha) and airborne LiDAR datasets (approx. 1-10⁴ km²) (Réjou-Méchain et al.,
107 2019; Oehmcke et al., 2022). With a surveying accuracy comparable to field-based measurements, UAV LiDAR mon-
108 itoring provides datasets (i.e. point cloud data, PCD) that allow high throughput individual tree phenotyping at an
109 intermediate spatial scale (approx. 1-40 ha).

110 While it is commonly argued that understanding local ecological processes in forests requires monitoring metrics
111 (e.g. structure, biomass) of individual trees (Potvin and Dutilleul, 2009; Ratcliffe et al., 2015; Zhang et al., 2020; Xu
112 et al., 2021), the reverse perspective is seldom discussed: how and to what extent can community ecology processes
113 be harnessed in tree-level regression experiments? Earlier works have proposed to account for the effects of imme-
114 diate competition pressure on tree growth with either distance-based (Lo and Lin, 2012) or distance-independent
115 metrics (Biging and Dobbertin, 1995; Sun et al., 2019), generally finding such approaches beneficial to improve tree
116 level estimates (Sun et al., 2019; Zhang et al., 2020). However, these studies are based on the premise that compe-
117 tition indices are the determining factor conditioning tree development, while overlooking other potential regulation
118 factors. In this scenario, nonparametric ML regression methods, which do not assume preexisting distributions or
119 premises, are a sound approach to incorporate a contextual analysis, and have been proposed in previous forest map-
120 ping studies (Schiefer et al., 2020).

121 Context-based regression studies (Marques et al., 2011; Zhao et al., 2015) have shown in the last decade that the
122 inclusion of information of local context (i.e. information about the surroundings of the target object) may improve
123 model performance as a result of consistent spatial correlations (Chu et al., 2013). This information can be included in
124 a learning model by either enlarging the receptive field size (i.e. widening the field of view) (Luo et al., 2016; Yang et al.,
125 2017; Schiefer et al., 2020) or by incorporating context-aware features that encode neighboring information into the
126 target object (Liu et al., 2018), i.e. a specific tree in forestry applications. However, context-based studies typically
127 rely on deep learning architectures and large datasets (Schiefer et al., 2020), which may obfuscate the explainability
128 of model performance improvement, which make them suboptimal for ecological applications, where the focus is
129 on explaining regulation factors. In contrast, when interpretability and dataset size limitations are critical, shallow
130 learning methods (e.g. ensembles of decision trees and regularized linear models) are usually preferred (Mittal et al.,
131 2023; Jafari et al., 2024).

132 Here, we present a UAV LiDAR-based framework that combines ecological analysis of forest structural organisa-
133 tion with context-aware modelling of tree diameter and tree-level AGB across 33 ha of a mature Norway spruce forest,
134 in near-natural conditions. We first analyse gradients of tree height across the forest to delineate tree assemblages
135 and examine their morphology. This enabled an explicit assessment of relationships between tree-level attributes
136 (i.e. height) and assemblage-level characteristics. Building on this structural analysis, we then evaluate whether as-
137 semblage-derived information can be leveraged to improve predictions of tree diameter and AGB. Specifically, we
138 (i) acquired close-range UAV LiDAR point cloud data, (ii) quantified spatial associations of tree height to define tree
139 assemblages, (iii) characterised assemblage morphology as an indicator of forest structural organisation and ecolog-
140 ical similarity, and (iv) integrated tree assemblage metrics into pairs of twin regression methods that differ only in the
141 use of contextual information. We assessed prediction performance across three shallow learning methods and two

142 datasets from the same coniferous forest. The proposed approach relies exclusively on UAV LiDAR data, without
143 ancillary information or inventory-derived metrics, facilitating practical application.

144

145 2 | MATERIALS AND METHODS

146 2.1 | Study Area

147 The Seehornwald Davos research site ($46^{\circ} 48' 55.2''\text{N}$, $9^{\circ} 51' 21.3''\text{E}$, 1640 m a.s.l.) is located in a managed sub-
148 alpine coniferous forest on the western flank of the Seehorn mountain, near Davos, in the Swiss Alps. The site is
149 labeled as a class-1 forest Ecosystem station (CH-Dav) ([ICOS, 2026](#)) of the Integrated Carbon Ecosystem Station
150 (ICOS) network ([Heiskanen et al., 2022](#)) where regular forest inventory measurements are collected following stan-
151 dardized protocols. The site is covered by spruce trees (proportion of *Picea abies* (L.) Karst., > 99.5 %) with an average
152 height and age of 13 m and 84 years, respectively, while some trees reach a height of 40 m and an age of 350 years.
153 The stand parameters at the research site include tree density: approx. 1143 tree/ha; basal area: 41.9 m^2/ha ; mean
154 crown area of dominant canopy: 13.2 m^2 ; and mean diameter at breast height (DBH): 17.3 cm.

155 The study area has not been affected by infrastructure development during the 20th-21st centuries. Since 1930,
156 grazing livestock in the forest was abandoned, and the region is sustainably managed according to the Swiss Forest
157 Law (1876) ([Burri, 2019](#)). The history of the site ([Swiss FluxNet, 2024](#)) shows that it was selected as a research site
158 in 1985, and there has not been management activities or harvesting in the study area, except for a clearing event
159 in 2005 that partially affected one Sparse Measurement Plot (SP-6, Annex VI). Maps dating back to 1845 reveal
160 minimal changes within the Davos-Seehornwald forest site, while slight effects of local harvests and regrowth can be
161 observed at the timberline ([Burri, 2019](#)). Since 2005, only minimal tree removals have taken place (ca. 6 trees along the
162 road). Patchy vegetation (i.e. dwarf shrubs and mosses) covers around 30% of the forest floor (acidic ferralic podzols),
163 which lies on a mixed siliceous and dolomitic bedrock. The research site is part of national, e.g. [WSL \(1994\)](#), [TreeNet](#)
164 ([2023](#)), [Swiss FluxNet \(1997\)](#) and international research networks, e.g. [ICOS \(2008\)](#), [ICP Forests \(1985\)](#), [ILTER-Europe](#)
165 ([2007](#)). The study area spans over 33 ha (Figure 1, b) and the terrain conditions are representative of the Alps around
166 the Landwasser valley, i.e. a varying steepness of $23 \pm 14^{\circ}$. The site lies on the eastern flank of the valley, so most of
167 the slopes face west-southwest (mean slope aspect is 230° SW).

168 2.2 | UAV LiDAR Survey and Field-Based Measurements

169 We used a UAV-borne LiDAR system mounted to a DJI Matrice 600 Pro payload at a 90° pitch angle, and same
170 heading and roll as the UAV platform. The system included a discrete return infrared LiDAR scanner (M8 sensor,
171 Quanenergy Systems, Inc. Sunnyvale, CA, USA) and the corresponding state-of-the art inertial and navigation systems.
172 In addition, we used a ground based Global Navigation Satellite System (GNSS, Trimble R8) during the UAV LiDAR
173 survey, set up in post-positioning kinematic (PPK) mode, which logged real-time satellite coverage (see [Revenga et al.](#)
174 ([2022](#)) for details on the UAV and ground systems). The coupling of the satellite coverage data with the UAV-based
175 laser and navigation data allowed the generation of georeferenced point clouds, following [Davidson et al. \(2019\)](#).

176

177 Data were acquired with a UAV flight height adapted to the terrain and tree height (Figure 2, a), ensuring a >20%
178 overlap between individual LiDAR scans of approx. 50 m width and $250 \text{ points}/\text{m}^2$. For each flight, the survey was per-
179 formed at a fixed height above the take-off point. The surveys were conducted in October 2021, coinciding with the

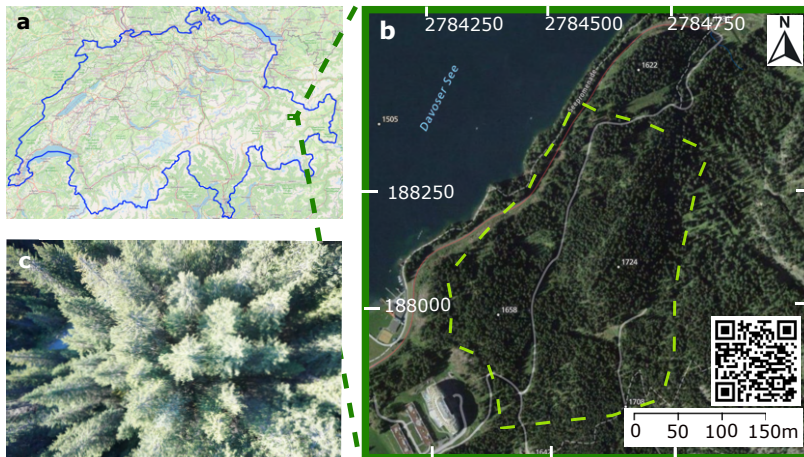


FIGURE 1 a: Location of the study site; the blue outline delineates the national territory of Switzerland (adapted from open.sourcemap.com). b: Orthoimage of the study site (adapted from swisstopo.admin.ch); coordinate units are in m (CH1903 / LV03 as the reference system); the QR code links to additional information of the study site. The dashed yellow line shows the boundaries of the study area. c: Sample photo from UAV.

end of the growing season. Figure 2 (a) shows the trajectories of the UAV LiDAR flights during the survey campaign. While the standard survey coverage followed a regular auto-pilot flight grid, certain flight lines had to be manually piloted to adapt to sudden topographic features and canopy structure. The digital elevation model of the study area is provided in Annex VI, to help understand differences in flight heights.

184

The field-based measurements (shown in Figure 2, b) are taken on a yearly basis as part of a long-term ecosystem monitoring initiative—jointly organized by ICOS ([ICOS, 2008](#)) and the Swiss Federal Institute for Forest, Snow and Landscape Research ([WSL, 1994](#)). Following a standardized protocol ([WSL, 1985](#)), expert field workers monitor tree crown status, focusing on three groups of indicators: variations in size, density and color. The number of trees that have died since the previous survey, as well as the new ones that reached a minimum DBH of 5 cm are also recorded. Tree height and DBH are monitored with a high-precision digital rangefinder (i.e. Vertex Laser Geo) and a standard calliper, respectively.

192

We treated two different datasets separately as ground truth measurements within the same study area: Continuous Monitoring Plot trees (CP-trees, 4 adjacent monitoring units), and Sparse Measurement Plot trees (SP-trees, 20 scattered units of 15 m radius). The two datasets (i.e. CP- and SP-trees) are monitored by different research groups on the field and protocols presented minor differences. Two main factors led us to consider both datasets separately: (i) the CP-dataset is clustered and spatially continuous, while the SP-dataset is spatially discontinuous and distributed along the study site (Figure 2, b); and (ii) the two datasets present differences in morphological trait distribution (Annex V). Figure 2 (b) shows the spatial distribution of the field-based forest inventory. The CP tree position was recorded using a Leica GPS1200 total station. The location and size of the sampling plots were defined according to ICOS protocols ([Gielen et al., 2018; ICOS, 2019](#)). The center location of the SP plots was determined using a GNSS Leica CS20 (antenna GS15) with a real-time kinematic (RTK) signal (accuracy measurements ranges from 0.03 m to 0.7 m). Next, the trees in the SP plots were positioned by measuring the azimuth with a field goniometer, while the horizontal distance of each tree and the inclination from the plot centers was determined using a Vertex Laser Geo meter. The

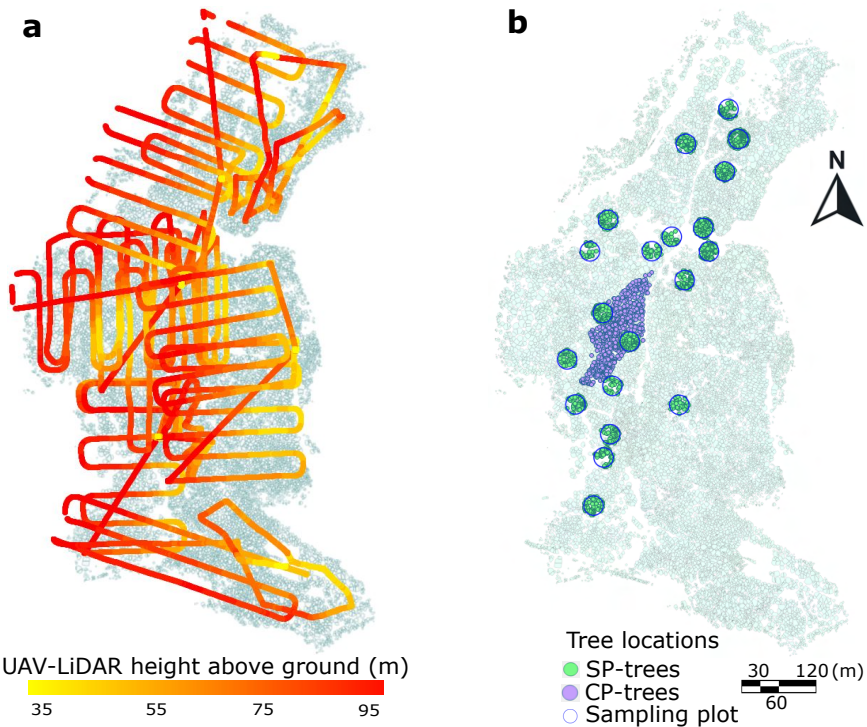


FIGURE 2 a: Trajectories of individual flights during survey of the Unstaffed Aerial Vehicle (UAV) Light Detection and Ranging (LiDAR) sensor; color gradient indicates height above ground during survey. Only the trajectories during LiDAR data acquisition are shown (take off and landing trajectories were omitted); the flight height (fixed above take-off point) shows the difference between the horizontally stable UAV survey and the variable terrain elevation. b: Spatial distribution of field-based forest inventory. Dots represent the locations of the ground truth labels. The Sparse Measurement Plot-trees (SP-trees, N = 1616 trees) are shown in green; the Continuous Measurement Plot-trees (CP-trees, N = 758 trees) are shown in purple. In both a and b, the underlying polygon dataset shows the individual tree canopies after the canopy height model segmentation.

accuracy of foot location of trees in the SP plots is within 0.5 m and 1.2 m. The field-based inventories used as ground truth contain measurements taken between October 2019 and July 2021. The changes in structural traits between the time of field-based measurements and UAV LiDAR data acquisition were considered negligible for the purposes of this study and no major disturbance events were registered during this period.

2.3 | Method setup

The workflow we followed is presented in Figure 3. Initially, the PCD generation followed the approach described in Revenga et al. (2022) (Revenga et al., 2022). The resulting PCD scene was normalized and rasterized to obtain a canopy height model (CHM), which in turn was subject to individual tree crown segmentation producing a two-dimensional polygon dataset. For the CHM segmentation, we utilized the watershed algorithm of Chen et al. (2006) (Chen et al., 2006). The match between field-based measurements and individual tree crown polygons was conducted based on the closest distance between the field-based GNSS point measurement and the individual tree crown polygon cen-

215 troid.

216

217 In order to ensure that only the LiDAR-detected trees would be accounted for in the regression experiment, a
 218 pre-processing task was required (marked * in Figure 3, the details of the preprocessing tasks involved are given in
 219 Annex II). Afterwards, using the LiDAR-derived height as polygon attribute, we calculated the distance at which the
 220 spatial autocorrelation of tree height was most significant in order to define the optimal neighborhood size (Section
 221 3.1). Once the optimal neighborhood size was defined, we conducted the local indicators of spatial association (LISA)
 222 analysis (Anselin, 1995; Anselin and Rey, 2010) and outlier analysis (Breunig et al., 2000; Liu et al., 2008) to retrieve
 223 neighborhood metrics. Finally, two separate supervised regression experiments were performed, in order to predict
 224 DBH based on LiDAR-derived metrics: one including the neighborhood metrics (context-aware regression), the other
 225 without taking those metrics into account (context-unaware regression). Finally, AGB was estimated from the pre-
 226 dicted DBH via an allometric function (as defined in Eq. 5).

227

228 In parallel, we evaluated the morphometry of the tree assemblages. Prior to the morphometric analysis of tree
 229 assemblages, a second pre-processing task was conducted on the individual tree crown dataset, where single crowns
 230 were merged, and inner borders were discarded (Annex II).

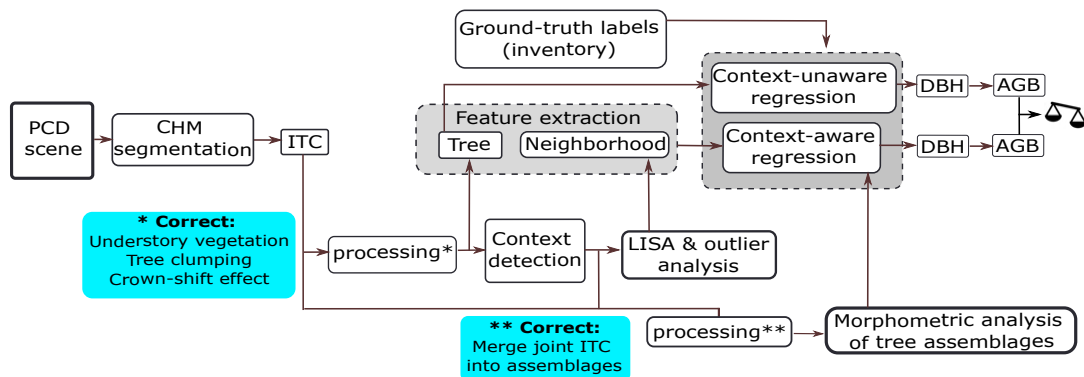


FIGURE 3 Workflow followed in this study. PCD: point cloud data, CHM: canopy height model, ITC: individual tree crown, LISA: local indicators of spatial association, DBH: diameter at breast height, AGB: aboveground biomass. The two blue boxes describe the subtasks constituting each of the processing steps, marked * and ** in the diagram.

231 | Defining Spatial Context from Tree Heights

232 We determined the distance at which neighborhood metrics should be calculated (i.e. how many surrounding trees
 233 should be accounted as neighbors) based on local similarity of tree height. Accordingly, the selection of an appropriate
 234 neighborhood size around each individual tree (i.e. context detection) was calculated through the analysis of spatial
 235 autocorrelation of tree height as function of incremental distance. Based on the global peak in the significance of
 236 spatial autocorrelation, we defined a characteristic distance within which all included trees should be considered as
 237 neighbors. Then, all so-defined neighbor trees were accounted for to compute context-aware metrics.

238

239 This context information was encoded as metrics derived from the distance-weighted neighbor tree heights cal-
 240 culated at each tree location. Specifically, the metrics computed to define the local context were: local Moran's I (i.e.
 241 an estimate of local significance of tree height similarity with respect to the global variance); and spatial lag of tree
 242 height (i.e. a weighted average of heights calculated entirely locally) (Anselin et al., 2009).

243

244 Local Moran's I_i is a well-established distance statistic in spatial data analysis (Cressie, 2015), used for detecting
 245 local spatial autocorrelation and included within the family of LISA methods (Anselin, 1995; Anselin et al., 2009;
 246 Anselin and Rey, 2010). Similarly to other geostatistics methods (Getis and Ord, 2010), it relates attribute similarity
 247 with locational similarity, mapping autocorrelation across the geographic space. In the following definitions, σ is the
 248 global sample standard deviation of tree height; n and m represent the total number of instances (i.e. all trees in the
 249 forest) and the number of neighbors to each tree, respectively; y_i indicates the magnitude of interest at a particular
 250 point of interest (i.e. tree height) while the overline (i.e. \bar{y}) indicates the global average; $w_{i,j}$ indicates the distance
 251 weighting of each neighboring tree (here defined as inverse distance weighting); subindexes i and j indicate the tree
 252 of interest and a neighbor tree, respectively. Let y_1, \dots, y_n be the tree height values of all the n trees in the dataset.
 253 Then, the Local Moran's I_i (Anselin, 1995) is defined as

$$I_i = \frac{y_i - \bar{y}}{\sigma^2} \sum_{j \in N_i, j \neq i} w_{i,j} (y_j - \bar{y}), \quad (1)$$

254 where $N_i \subset \{1, \dots, m\}$ is the set of indices corresponding to the nearest neighbors of tree $i \in \{1, \dots, n\}$ in the
 255 overall set, where

$$\bar{y} = \frac{1}{n} \sum_{i=1}^n y_i, \quad (2)$$

256 and

$$\sigma = \sqrt{\frac{\sum_{i=1}^n (y_i - \bar{y})^2}{n - 1}}, \quad (3)$$

257 are the global average height and the global sample standard deviation, respectively. It should be noted that inso-
 258 far I_i includes global metrics (such as n , σ and \bar{y}), it is not entirely locally computed, but may present correlation with
 259 global features (i.e. characteristics derived from the entire dataset; cf. Westerholt et al. 2018) (Westerholt et al., 2018).

260

261 The Spatial Lag (SL_i) of tree height for a tree i is a spatial smoother defined as

$$SL_i = \sum_{j \in N_i, j \neq i} w_{i,j} y_j \quad (4)$$

262 where the elements of the spatial weights matrix ($w_{i,j}$) are row-standardized, so that $\sum_{j \in N_i, j \neq i} w_{i,j} = 1$. Therefore,
 263 SL_i can be seen as a weighted average of the heights of neighboring trees (Anselin et al., 2001).

264

265 The neighborhood metrics finally chosen as context-aware predictors are the following: local Moran's Index (I_i),
266 z-score of I_i , p-value of I_i , z-transformed value of I_i and SL_i —computed at 20 m, 30 m, 40 m and 50 m distance
267 bands. Additionally, the mean heights of the k-nearest trees, with $k \in (5 - 75)$, were also included as predictors.
268 Likewise, we also included the topographic wetness index (TWI) (Beven and Kirkby, 1979) in order to evaluate the
269 relative predictive performance of neighborhood metrics with respect to a well-established environmental variable as
270 tree-growth predictor (Mohamedou et al., 2017) (Annex VII).

271

272 Finally, we included in the regression experiments predictive features informing of local neighbor dissimilarity, i.e.
273 local outliers of tree height. We detected local outliers using Local Outlier Factor (Breunig et al., 2000) and Isolation
274 Forest (Liu et al., 2008) algorithms. The evaluation of these features allowed us to discern between the contribution
275 of local similarity features (i.e. Local Moran's I_i and SL_i) and that of the local outliers.

276

| Forest Structure

277 In order to define the tree assemblages, both local Moran's I_i and SL_i were computed at the optimal distance band to
278 obtain neighborhood metrics, i.e. based on the global peak in the significance of spatial autocorrelation of tree height
279 as a function of distance (using ArcGIS Pro) (ESRI, 2021).

280

281 Tree assemblages were therefore defined as geographically continuous groups of trees delineated according to
282 either (i) variation of local Moran's I_i of tree height, or (ii) according to quantiles of SL_i of tree height. The rationale
283 for using two different statistics to calculate tree neighborhood metrics and thus delineate different tree assemblages
284 is that while SL_i is entirely locally calculated, local Moran's I_i includes global features (and is therefore sensitive to
285 the statistical characteristics of the dataset as a whole, Section 2.3). In order to discern which of the two approaches
286 resulted most convenient to delineate tree assemblages (the former *entirely local*; the latter only *partially local*), both
287 were included.

288

289 Tree assemblages defined according to local Moran's I_i are geographically continuous groups of trees with signif-
290 icantly different heights than the global tree height average, and they also lie in a region with significantly different
291 neighbors. Local Moran's I_i identifies regions where the clustering of either high or short trees occurs. In the standard
292 notation (Anselin et al., 2009) (i.e. High-High or Low-Low), the first term refers to the individual tree and the second
293 to the neighborhood (e.g. a tree belonging to a High-High assemblage is a "significantly high tree" in a "significantly
294 high neighborhood"). The areas not showing statistical significance (a p-value ≥ 0.002 was considered sufficient) were
295 labeled as Not-Significant. The significance test is based on random permutations ($n = 499$) of neighboring tree-height
296 values at each step in the computation. The number of permutations and p-value indicate that, under the null hypoth-
297 esis (i.e. tree heights being randomly distributed), a single tree canopy may be wrongly classified with a probability of
298 0.002, which was deemed sufficient for the purpose of evaluating tree assemblage morphometry (i.e. if 1 out of 499
299 trees is wrongly attributed to a neighborhood, the morphometry of the assemblage will not change markedly). Then,
300 for every permutation, a local Moran's I_i value was calculated by randomly rearranging the tree heights of neighboring
301 values. The result is a randomly generated reference distribution of expected local Moran's I_i that is compared against
302 the observed local Moran's I_i (Eq. 1) (Anselin and Rey, 2010). In this way, tree assemblages defined according to local
303 Moran's I_i are classified as: High-High, Low-Low, or Not-Significant.

304

305 Likewise, tree assemblages defined according to SL ; of tree height are geographically continuous groups of trees
306 delimited according to the local weighted average of tree height (Anselin et al., 2001), as defined above (Eq. 4). For
307 the purpose of this study, 5 subdivisions based on quantiles were deemed convenient, rendering a classification of
308 tree assemblages based on SL ; ranking as: *Highest, High, Mid, Low and Lowest*.

309

310 The morphometric analysis examined the outer boundaries of the tree assemblages as defined above. Twenty
311 basic morphometric parameters as well as 20 derived parameters were calculated for each type of tree assemblage.
312 The 20 basic morphometric variables are simple parameters obtained by fitting elemental geometric shapes to each
313 tree assemblage polygon (e.g. area of maximum inscribed circle), and basic positional parameters (e.g. XPOL, which
314 is the X coordinate of the centroid of the tree assemblage polygon). The 20 derived parameters are adimensional
315 metrics (except for concavity (Landini, 2010), measured in m^2) computed from the 20 basic morphometric variables,
316 as explained in Güler et al. (2021) (Annex III). The morphometric analysis of tree assemblages was conducted using
317 PolyMorph-2D algorithm, available as a plug-in for the open source JUMP GIS software (Steiniger and Blake, 2022).

318

319 | Regression Models Selected

320 The regression experiments were designed to predict DBH, since AGB is a variable determined by the combination
321 of DBH, height and wood density (Dalponte and Coomes, 2016). In contrast, DBH is directly measured in the field,
322 which makes it a better defined regression target. Therefore, the model estimates of AGB were derived from the DBH
323 prediction outputs by means of an allometric fit (Eq. 5). Predicting DBH, instead of AGB directly was chosen as more
324 suitable, as it avoids burdening the learning models with the statistical error contained in the allometric fit. Three
325 feature-based shallow learning regression methods were selected: namely AdaBoost (Freund and Schapire, 1997;
326 Friedman, 2001; Schapire, 2013), Lasso (Tibshirani, 1996) and Random Forest (Ho, 1995) regressors. The AdaBoost
327 regressor is a tree-based gradient-boosting method that relies on stage-wise additive expansions. Its effectiveness
328 stems from combining weak learners to form a generalized prediction hypothesis. Lasso is a linear model that applies
329 an L1-norm penalty for regularization (Vidaurre et al., 2013). Finally, Random Forest is a well established tree-based
330 ensemble regression method. All three shallow regression methods utilize the features derived from the individual
331 tree crown polygon dataset resulting from the CHM segmentation.

332

333 Context-unaware regressions were defined as those in which a learning model performs DBH regression by tak-
334 ing as predictors only individual tree attributes derived from the ITC polygon dataset (i.e. tree height, canopy area
335 and canopy perimeter), as it is a common approach (Yao et al., 2014). On the other hand, we defined context-aware
336 regressions as those regressions in which contextual features are additionally introduced as predictors. These were
337 either neighborhood metrics (e.g. SL ; of tree height) or TWI at different spatial resolutions (Section 2.3). For every
338 model predicting DBH from individual tree attributes (i.e. context-unaware conditions) we implemented a context-
339 aware counterpart. This allowed us to evaluate the impact of context on regression performance.

340

341 | Model Training and Validation of Results

342 A direct validation of AGB is not possible without harvesting trees destructively, which raises obvious ethical, legal and
343 economic issues. Instead, non-invasive methods that use remote sensing data and allometric functions are the stan-

344 dard procedure for estimating AGB ([Gielen et al., 2018](#)). Here, we estimated AGB from tree height, DBH, wood density
 345 and an allometric function of Norway spruce trees (Eq. 5). Therefore, the regression analyses conducted focused on
 346 comparing performance of predictions on DBH between twin shallow learning methods (i) "context-unaware" and
 347 their (ii) "context-aware" counterparts. As independent ground reference to compare against, we used inventory-
 348 based DBH.

349

350 We chose DBH as the variable to test model predictions, which is included in the field-based forest inventory,
 351 and therefore directly measured by *in situ* monitoring. Next, in order to assess the benefits of including context in the
 352 regression models, we compared results using AGB of individual trees. Specifically, AGB estimates were derived via
 353 species-specific allometric and wood density functions, tree height retrieved via UAV LiDAR, and DBH predicted via
 354 ML regression. The allometric model used was the one proposed by [Dalponte and Coomes \(2016\)](#):

$$AGB_{tree} = \alpha \cdot WD_{spruce}^{\beta} \cdot (DBH - d_0)^{\gamma} \cdot H^{\delta}, \quad (5)$$

355 where the wood density value (WD_{spruce}) was taken from Alpine spruce dendrometric models ([Gryc and Horáček,](#)
 356 [2007](#)), DBH was predicted via ML regression and height (H) was extracted from the UAV LiDAR acquisition. $\alpha, \beta, \gamma, \delta$
 357 and d_0 are species-specific fitted allometric parameters ([Scrinzi et al., 2010](#)), obtained from allometric fits to harvested
 358 spruce trees by the Forestry and Wildlife Service Agency of the province of Trento (Italian neighbouring province
 359 southeast from the study site, also used in Dalponte and Coomes, 2016), and we consider them applicable to the See-
 360 hornwald Davos research site. At all events, for the purpose of assessing the benefits of a context-aware approach,
 361 the specific characteristics of the allometric fit used are trivial, as it is only used to quantify a difference in terms of
 362 AGB, and both types of predictions (in either aware or unaware conditions) take the same equation. Therefore, the
 363 predicted value of DBH was input into Eq. 5, in order to obtain model predictions of AGB. This allowed to compare
 364 AGB predictions with the ground truth values of AGB, which were similarly obtained via the field-based measure-
 365 ments of DBH and height (provided by the regular tree-monitoring campaigns of ICOS ([ICOS, 2008](#)) and WSL ([WSL,](#)
 366 [1994](#))), and Eq. 5.

367

368 The technique used to estimate model prediction error consisted of a nested cross-validation (NCV, Annex IV)
 369 scheme adapting the procedure from Bates et al. (2021) ([Bates et al., 2021](#)). Following the NCV scheme, the dataset
 370 was partitioned into 10 random outer folds, which are mutually exclusive. For each outer iteration, one outer fold was
 371 held out as an independent test set, while the remaining nine folds formed the training set. This training set was further
 372 partitioned into 5 mutually exclusive inner folds, over which a 5-fold cross-validation was performed to tune model
 373 hyperparameters and select the optimal model configuration. Inner-fold validation performance was used exclusively
 374 for model selection, while performance obtained on each outer test fold was retained as an independent estimate of
 375 generalization error. The model inspection technique used to evaluate predictors' influence on the DBH regression
 376 results was the permutation importance method as proposed by Altmann et al. (2010) ([Altmann et al., 2010](#)). Permu-
 377 tation importance was computed on the outer test folds only, to avoid information leakage. The feature-elimination
 378 procedure consisted of eliminating progressively those predictors that presented a negative mean importance, with
 379 feature removal performed within the NCV training process, as they were considered harmful to the model's per-
 380 formance. The significance of the enhancement in context-aware predictions and effect size was assessed using Wilcoxon
 381 signed-rank test ([Wilcoxon, 1992](#)) and Cliff's Delta analysis ([Cliff, 1993](#)), respectively. Outer-fold performance scores
 382 were treated as paired samples, forming empirical performance distributions for the context-unaware and context-

383 aware models, respectively. Statistical tests were applied to these paired outer-fold results, using corresponding folds
 384 as matched observations.

385 3 | RESULTS

386 3.1 | Context Detection and Forest Structure

387 The analysis of spatial autocorrelation of tree height as function of incremental distance resulted in a maximum sig-
 388 nificance at a distance of 40 m. Figure 4 (a) shows the calculation of local Moran's index (I_i) of tree height at different
 389 distance bands. Figure 4 (b) shows the standard score (i.e. z-score) of I_i obtained at each distance band, resulting
 390 from comparing the observed I_i and the expected I_i under the tree height randomness assumption (Annex I). As a
 391 precaution, we ran context-aware regression experiments including also context features retrieved at shorter (i.e. 20
 392 m, 30 m) and larger (i.e. 50 m) distances than the optimal range (i.e. 40 m). The context features retrieved at these
 393 distances (i.e. 20, 30, 40 and 50 m) which contributed to improve the predictions of DBH were all included in the final
 394 regression models.

395

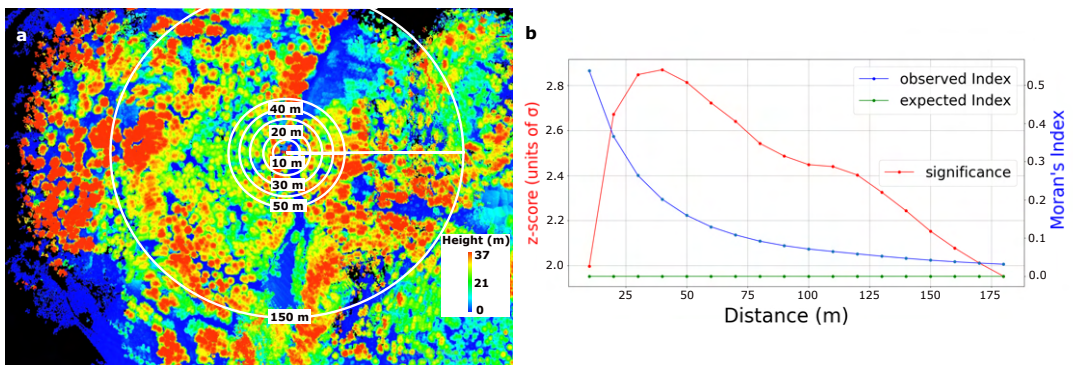


FIGURE 4 Context detection. **a:** Normalized point cloud data (PCD) scene colored by tree height overlaid with a selection of the appropriate radii for defining the neighboring context. **b:** Autocorrelation of tree height as function of distance. The red line shows the number of standard deviations (σ) that an observation is away from the expected value (under the assumption of heights being randomly distributed). The blue and green lines show the actually observed local Moran's Index and the expected value under randomness assumption, respectively.

396 In Figure 5, panels a and b show the spatial distribution of tree assemblages calculated using either local Moran's
 397 I_i or SL_i of tree height, respectively, at 40 m range. While both types of assemblages show similarities as regards
 398 extent, morphometry and location, SL_i captures more local variability, resulting in more small, localized clusters. This
 399 is not only due to a higher discretization (5 clusters in SL_i , vs. 3 clusters in local Moran's I_i), but also to the fact that
 400 SL_i is not sensitive to the variance in the dataset beyond the range of its neighborhood (as explained in Section 2.3).

401

402 The morphometric analysis provided 40 additional features that were evaluated as potential predictors of DBH. In
 403 Figure 6, panels a and b visualize the results of the morphometry analysis of tree assemblages defined by local Moran's
 404 I_i and by SL_i , respectively. The circular barplots show the average magnitude as bar lengths, and the standard devi-

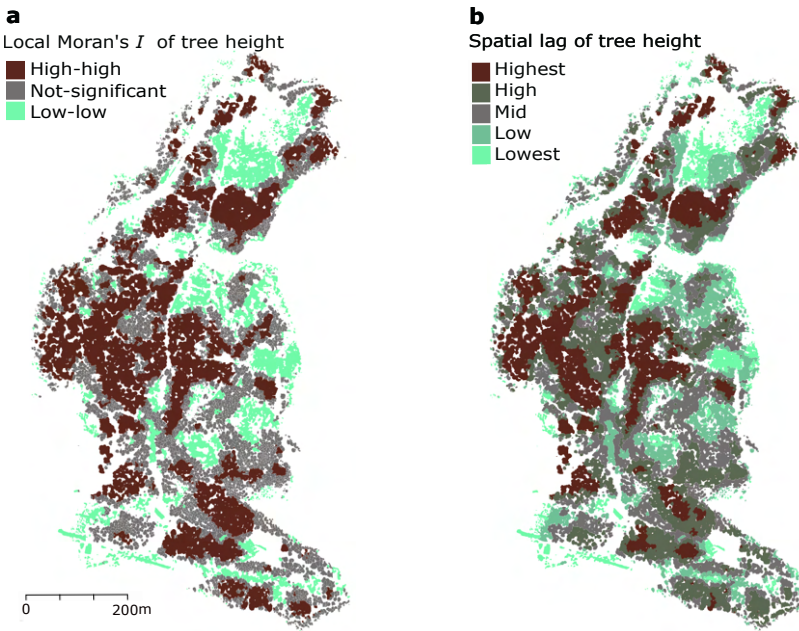


FIGURE 5 Tree assemblages defined by local similarity of tree height. **a:** Delineated according to local Moran's I_i of tree height. **b:** Delineated according to spatial lag of tree height (SL_i).

ation as dots. Both mean and standard deviation values are shown as min-max scaled (across assemblage types) to present all variables on the same radial axis and to ease visual comparison, i.e. for every morphometric variable, the highest value is replaced by 1, the minimum is replaced by 0, and the intermediate values are linearly interpolated between 0-1. It can be observed that the morphometric variables follow very similar trends when tree assemblages are defined based on local Moran's I_i or SL_i . However, an observed difference between SL_i and local Moran's I_i was found in the heteroscedasticity of the morphometric variables calculated, where only in the former case variance of all metrics scaled with magnitude.

412

While not for all variables a systematic trend was found, for several basic morphometric variables a linear positive correlation between them and SL_i was observed, as shown by the Pearson coefficient (ρ). This is the case for polygon area ($\rho=0.95$), perimeter of polygon (PPOL; $\rho=0.98$) and radius of the minimum circumscribed circle (RMCC; $\rho=0.98$). Additionally, a positive correlation was found for some derived morphometric variables, namely: length-to-width ratio (LTWR; $\rho=0.75$) (Horton, 1932), circularity ratio (CIRR; $\rho=0.88$) (Attnave and Arnoult, 1956), compactness factor (COMF; $\rho=0.89$) (Güler et al., 2021), dispersion measure (DISM; $\rho=0.90$) (Attnave and Arnoult, 1956), complexity index (COMI; $\rho=0.88$) (Güler et al., 2021), lemniscate ratio (LEMR; $\rho=0.81$) (Chorley et al., 1957), regularity factor (REGF; $\rho=0.82$) (Buendia et al., 2002), and concavity (CONC; $\rho=0.96$) (Landini, 2010). Conversely, other morphometric variables showed a decreasing trend with increasing SL_i . A clearly negative correlation between SL_i and the following derived morphometric variables was found: Miller's circularity ratio (MCIR; $\rho=-0.88$) (Miller, 1953), Horton's form factor (HFOR; $\rho=-0.88$) (Horton, 1932), elongation factor (ELOF; $\rho=-0.83$) (Schumm, 1956), shape factor (SHAF; $\rho=-0.95$) (Buendia et al., 2002), rectangularity (RECT; $\rho=-0.85$) (Rosin, 1999) and roundness (ROUN; $\rho=-0.69$) (Horgan and Glasbey, 1995). More details are given in Annex III (Figure 12).

425

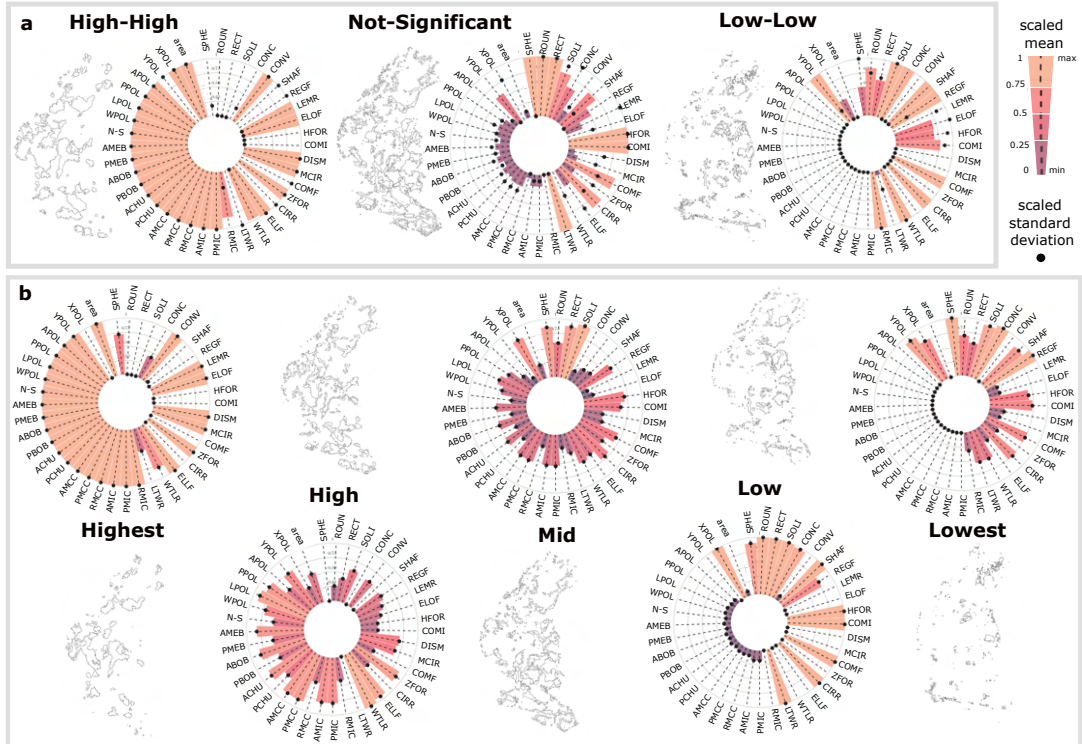


FIGURE 6 Morphometric analysis of tree assemblages grouped by (a) local Moran's I_i , and (b) by spatial lag of tree height. Bar length and color gradient represent the mean value, while black dots represent the standard deviation (SD) over all tree assemblages. Both mean and SD are scaled (min-max) to allow comparison of all metrics across assemblage types on the same axis—i.e. for every morphometric variable, the highest value of a certain assemblage type is replaced by 1, the minimum value is replaced by 0, and the intermediate values are linearly interpolated in between the range (0-1). YPOL: northing of centroid of the tree assemblage; XPOL: easting of centroid of the assemblage; APOL: area of polygon (P); N-S: defined as $|\sin(\text{azimuth})|$, shows the alignment of the main axis of P with the North-South direction; PPOL: perimeter of P; LPOL: major axis length (L) of P; WPOL: minor axis length (W) of P; ABOB: area of the bounding box fully containing P; PBOB: perimeter of the bounding box fully containing P; AMEB: area of the minimum enclosing box fully containing P; PMEB: perimeter of the minimum enclosing box fully containing P; ACHU: area of containing hull ; PCHU: perimeter of convex hull fully containing P; AMCC: area of the minimum circumscribed circle (MCC); PMCC: perimeter of MCC; RMCC: radius of MCC; AMIC: area of maximum inscribed circle (MIC); PMIC: perimeter of MIC; perimter of MCC; RMIC: radius of MCC; LTWR: length-to-width ratio (Horton, 1932); WTLR: width-to-length ratio (Zingg, 1935); ELLF: ellipticity factor (Buendia et al., 2002); CIRR: circularity ratio (Attnave and Arnoult, 1956); ZFOR: Zavoianu's form factor (Zăvoianu, 1978); COMF: compactness factor (Güler et al., 2021); MCIR: Miller's circularity ratio (Miller, 1953); DISM: dispersion measure (Attnave and Arnoult, 1956); COMI: complexity index (Güler et al., 2021); HFOR: Horton's form factor (Horton, 1932); ELOF: elongation ratio (Schumm, 1956); LEMR: lemniscate ratio (Chorley et al., 1957); REGF: regularity factor (Buendia et al., 2002); SHAFF: shape factor (Buendia et al., 2002); CONV: convexity (Horgan and Glasbey, 1995); CONC: concavity (Landini, 2010); SOLI: solidity (Zunic and Rosin, 2004); RECT: rectangularity (Rosin, 1999); ROUN: roundness (Horgan and Glasbey, 1995); SPHE: sphericity (Wadell, 1935). Correlation coefficients of the most prominent variables are given in Annex III.

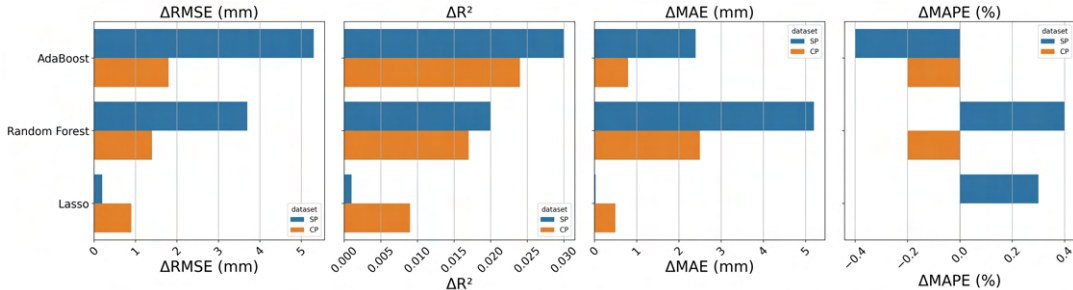


FIGURE 7 Enhancement of predictions of diameter at breast height per model type as a result of including context-based predictor variables (zero-reference corresponds to the prediction performance without including context-based predictors). MAPE: mean absolute percentage error.

426 3.2 | Tree diameter Regression: Aware vs. Unaware of Local Context

427 Regression experiments including context-aware features improved predictions of DBH consistently (Figure 7, Ta-
 428 bles 1 and 2), resulting in enhanced tree-level AGB predictions via allometry (Eq. 5). We found a general trend across
 429 methods of improved prediction performance w.r.t R², RMSE and MAE in both SP- and CP-datasets. For each pairwise
 430 comparison, the improvements were consistent, although the degree of prediction enhancement differed between the
 431 two datasets considered. Predictions in the CP-dataset observed a lower enhancement in comparison to predictions
 432 in the SP-dataset. For instance, with AdaBoost, RMSE was reduced by 4.1% (SP-dataset) vs. 0.8% (CP-dataset), with
 433 a corresponding improvement observed in R² values, i.e. by 0.03 (SP-dataset) vs. 0.024 (CP-dataset). This contrast
 434 between the sparse (SP) and continuous (CP) datasets suggests that the lower contextual variability in the CP dataset
 435 limits the added value of context features, whereas higher contextual variability in the SP dataset makes their contri-
 436 bution more effective.

437

438 Figure 8 (a) shows the ground truth labels (i.e. field based estimates of AGB), which were derived from the
 439 field measurements and the allometric fit (Eq. 5). The central panel (b) shows the spatial distribution of residuals (i.e.
 440 $\epsilon = AGB_{ground\ truth} - AGB_{prediction}$) of the AdaBoost context-aware regression results (i.e. the best performance).
 441 The mean values converge towards zero (i.e. $\bar{\epsilon}_{SP} = 3.8 \text{ kg}$, $\bar{\epsilon}_{CP} = -3.2 \text{ kg}$), while the spread of the error distribution
 442 varies between SP and CP-datasets (i.e. $\sigma(\epsilon_{SP}) = 123 \text{ kg}$, $\sigma(\epsilon_{CP}) = 140 \text{ kg}$). Figure 8 (b) also shows a low spatial auto-
 443 correlation of errors (i.e. low clustering), indicating that predictions are not geographically biased. Figure 8 (c) displays
 444 the error distributions in both datasets. SP-errors show a unimodal distribution with a slight overestimation of DBH
 445 of 28 mm. CP-errors present a similar overestimation bias (25 mm) with a bimodal distribution (the second mode is
 446 located at 25 mm of underestimation). The second mode of the bimodal pattern in the CP-dataset may correspond
 447 to the more frequent occurrence of larger trees, which tend to be underestimated (Figure 8, c, lower panels). It can
 448 be observed that, generally, smaller and thinner trees tend to be slightly overestimated (i.e. in the first two quantiles)
 449 compared to the largest trees, which tend to be underestimated.

450

451 Figure 9 presents the analysis of the relative importance of all predictors considered in the context-aware DBH
 452 regression with the AdaBoost regression model. The analysis reveals that in both SP- and CP-datasets, the most impor-
 453 tant context-based predictors are the average heights of the 5, 10, and 15 nearest neighboring trees, outperforming
 454 some individual-tree metrics, such as the crown metrics.

455
456
457
458

TWI made a marginal contribution to enhanced predictions. Moreover, although modest, TWI exhibited a greater impact on improved predictive performance at finer spatial resolutions in both datasets (Figure 9), whereas its contribution decreased at coarser resolutions.

TABLE 1 Results (on test set) of the SP-dataset, for each pairwise model comparison (aware vs. unaware of context features). Predictor variables are entirely LiDAR-derived; the target variable is diameter at breast-height (DBH, in mm). The values are presented as mean \pm standard deviation of the 10 outer CV folds of the nested scheme. One asterisk (*) marks results where the enhancement introduced by context-awareness is statistically significant with "small" size effect, while ** and *** mark "medium" and "large" size effect, respectively. The best results are shown in bold. RMSE (%) is the error relative to the median DBH (125 mm). MAPE: mean absolute percentage error.

Regression model	R ²	RMSE (mm) / %	MAE (mm)	MAPE (%)
AdaBoost (unaware)	0.830 \pm 0.05	58.0 \pm 9.0 / 46.4 \pm 7%	43.3 \pm 4.4	19.1 \pm 1.9
AdaBoost (aware)	0.860 \pm 0.03 ***	52.7 \pm 5.3 *** / 42.1 \pm 4%	41.0 \pm 3.1 **	19.5 \pm 1.7
Random Forest (unaware)	0.818 \pm 0.04	60.2 \pm 7.3 / 48.1 \pm 6%	46.8 \pm 4.5	22.8 \pm 5.8
Random Forest (aware)	0.838 \pm 0.05 *	56.5 \pm 9.2* / 45.2 \pm 7%	41.6 \pm 5.4 ***	22.4 \pm 5.1
Lasso (unaware)	0.851 \pm 0.02	54.6 \pm 4.9 / 43.6 \pm 4%	4.20 \pm 3.3	19.1 \pm 1.4
Lasso (aware)	0.852 \pm 0.02	54.4 \pm 4.9 / 43.5 \pm 4%	4.17 \pm 3.5	18.8 \pm 1.7

TABLE 2 Results (on test set) of the CP-dataset, for each pairwise model comparison (aware vs. unaware of context features). The predictive variables are entirely LiDAR-derived; the target variable is diameter at breast-height (DBH, in mm). The values are presented as mean \pm standard deviation of the 10 outer CV folds of the nested scheme. One asterisk (*) marks results where the enhancement introduced by context-awareness is statistically significant with "small" size effect. The best results are shown in bold. RMSE (%) is the error relative to the median DBH (220 mm). MAPE: mean absolute percentage error.

Regression model	R ²	RMSE (mm) / %	MAE (mm)	MAPE (%)
AdaBoost (unaware)	0.713 \pm 0.07	54.7 \pm 5.98 / 24.8 \pm 3%	43.0 \pm 5.26	15.5 \pm 2.4
AdaBoost (aware)	0.737 \pm 0.05 *	52.9 \pm 5.28 * / 24.0 \pm 2%	42.2 \pm 4.43 *	15.7 \pm 3.1
Random Forest (unaware)	0.688 \pm 0.07	57.0 \pm 5.9 / 25.9 \pm 3%	43.8 \pm 5.1	15.7 \pm 3.1
Random Forest (aware)	0.705 \pm 0.04	55.6 \pm 5.3 / 25.2 \pm 2%	41.3 \pm 5.5 *	15.9 \pm 4.3
Lasso (unaware)	0.741 \pm 0.09	51.3 \pm 6.6 / 23.3 \pm 3%	39.1 \pm 5.2	13.6 \pm 1.6
Lasso (aware)	0.750 \pm 0.08	50.4 \pm 5.9 / 22.9 \pm 3%	38.6 \pm 4.1	13.6 \pm 1.1

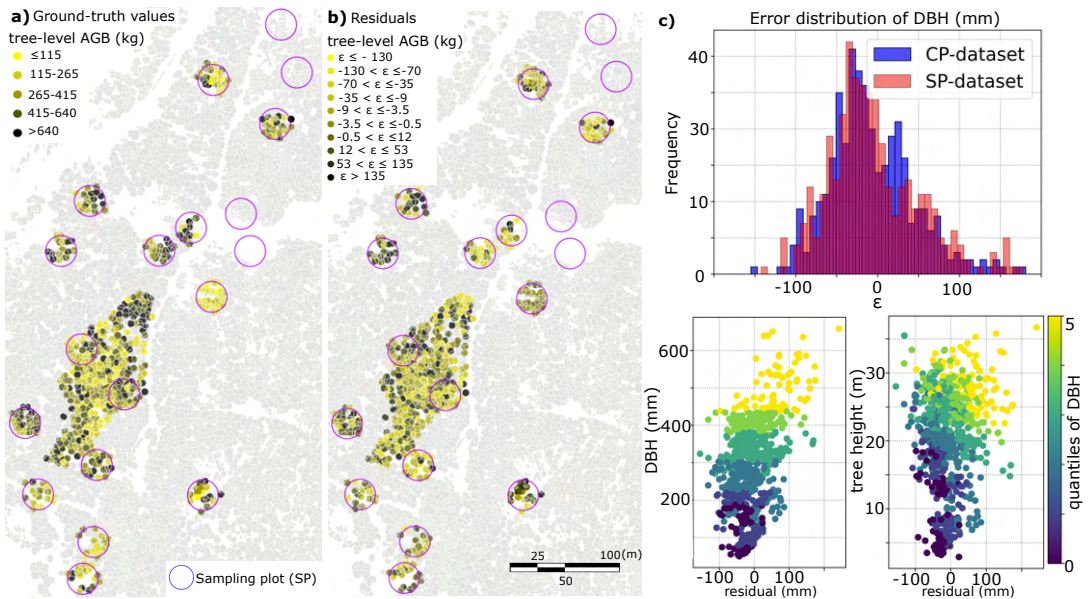


FIGURE 8 a: Spatial distribution of tree-level aboveground biomass (AGB) according to ground truth measurements. b: Spatial distribution of residuals ($\epsilon = AGB_{ground-truth} - AGB_{prediction}$) of AGB predictions with AdaBoost context-aware regression, grouped by quantiles (negative values indicate overestimation). The four empty SP-plots (and the southernmost one not included) correspond to areas where the quality of the UAV LiDAR data collection was compromised (Annex VI). c: Error distributions of diameter at breast-height (DBH) in Sparse Measurement Plot (SP) and Continuous Measurement Plot (CP) datasets. The two bottom-right panels show the residual distribution of DBH (in x-axis) vs. field-measurements of DBH and tree height (in y-axes). The color scheme refers to the quantiles of each dataset separately, which are differently distributed (Annex V).

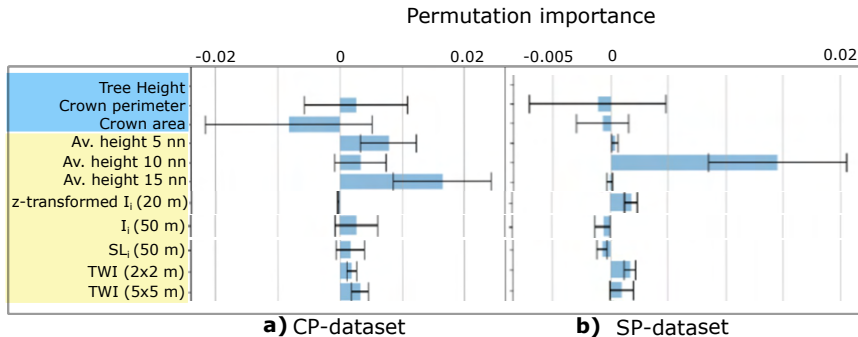


FIGURE 9 Inspection of predictors' permutation importance (Altmann et al., 2010) in the AdaBoost regression experiment in context-aware conditions. The left panel (a) shows results in the Control Plot (CP) dataset, and the right panel (b) shows results in the Sparse Measurement Plot (SP) dataset. Bar length and error bar show the mean and standard deviation of a predictor's importance, respectively. Predictors highlighted in blue are individual tree traits; predictors highlighted in yellow are context-based. In both datasets, it can be noted how the average heights of the 5–15 nearest neighbors (nn) stand out as the strongest predictors, outperforming crown perimeter and crown area. In both plots (a and b), individual tree height (with importance: 0.85 in CP-dataset; 1.3 in SP-dataset) has been removed to facilitate visual comparison of the remaining predictors. Only the 10 most significant predictors are included; an extended figure is shown in Annex VII.

4 | DISCUSSION

4.1 | Forest Structure

The analysis of morphometric variables for different tree assemblages (Figure 6) permitted to examine whether trees—grouped by local association of tree heights—persistently show different shapes at the group level, shedding light on the relationship between context-based traits (e.g. concavity of a tree assemblage) and single-tree heights. This analysis revealed certain patterns of trait convergence (Pillar et al., 2009), which was specially remarkable for some metrics, which showed a strong correlation with tree height, e.g. concavity (Landini, 2010) and length-to-width ratio (Horton, 1932).

Remarkably, it was observed that tree assemblages delineated according to the spatial lag of tree height (i.e. SL_i , Figure 6, b) presented clear positive correlations with two-dimensional morphometric features at the tree assemblage level. For instance, assemblages with higher trees (i.e. labeled as *Highest* according to SL_i , or *High-High* according to local Moran's I_i) are consistently rounder, larger and more regular in shape. As visualized in Figure 6, SL_i correlates positively with shape regularity (Buendia et al., 2002), concavity (Landini, 2010), length-to-width ratio (Horton, 1932) and size, indicating a consistent trait-convergence assembly pattern. Higher trees tend to converge in most sheltered areas (i.e. thalwegs and local sub-basins) so that tree assemblages with highest SL_i tend to adopt the morphological features of the drainage network's shape (Annex III). A more detailed interpretation of this observation, particularly in relation to tree assembly morphology, would warrant a dedicated follow-up study. However, it may indicate that both the shape and location of tree assemblages of different heights are conditioned by underlying environmental and biotic driving mechanisms.

In the coniferous forest studied here, a significant degree of clustering of tree heights takes place (Figure 5, a),

482 while spatial gradients of tree height present preferential shapes and directions (Figure 5, b). These observations
483 indicate that there is tree-height convergence and a tendency toward optimal phenotype expression (i.e. maximum
484 growth performance) around the runoff drainage network (Annex III, Figure 10). Higher trees are found in sheltered
485 regions and concave channels—which generally benefit from more frequent runoff events and deeper soils (Goebes
486 et al., 2019; Green and Keenan, 2022). This may indicate that favorable environmental conditions (e.g. deeper soil,
487 lower soil moisture recession rates, greater availability of soil nutrients due to leaching) allow individuals to reach their
488 optimal phenotype. Conversely, a lower SL_i of tree height in more exposed terrain (e.g. ridges, hilltops) may indicate
489 that environmental filtering (e.g. windstorm disturbance) or a reduced competition for light could play a significant
490 role in determining the location of low SL_i tree assemblages. Thus, the relatively reduced tree height in exposed
491 areas could indicate a passive adaptation of tree height to harsher environmental conditions (Valladares et al., 2007),
492 an active adaptation to higher light availability (Valladares et al., 2005a), a limitation to tree growth caused by other
493 local factors, such as lower soil depth or nutrients availability (Fatichi et al., 2019; Green and Keenan, 2022), or the
494 effect of these factors combined. Nevertheless, we cannot provide an interpretation of such observations, as shifts in
495 the variance of functional traits across environmental gradients, such as gradients of tree heights, do not bring strong
496 evidence of either biotic or environmental filtering on their own (Kraft et al., 2015).

497 4.2 | Enhancement of Tree Diameter and Aboveground Biomass Regression

498 Our context-aware shallow regression approach improved estimates of tree diameter and AGB in the studied sub-
499 alpine coniferous forest using UAV LiDAR data. These findings are consistent with established context learning liter-
500 ature (Marques et al., 2011; Chu et al., 2013; Zhao et al., 2015; Luo et al., 2016; Yang et al., 2017; Liu et al., 2018),
501 remote sensing trait mapping studies (Hao et al., 2020; Schiefer et al., 2020), and methodological advances on forest
502 modelling—namely, nonlinear mixed-effects methods (Yang et al., 2020; Liu et al., 2021) and competition-based stud-
503 ies (Lo and Lin, 2012; Sun et al., 2019; Zhang et al., 2020). We further extend this approach to a framework native
504 to UAV LiDAR systems. The pairwise comparison of methods consistently showed that context-aware regressions
505 outperformed context-unaware regressions across models (except for Lasso in the SP-dataset, where performance
506 stagnated, Tables 1 and 2), and in no case adding context information became detrimental. This finding may indicate
507 that gradients of tree heights across the ecosystem proxy for environmental and biotic mechanisms (e.g. windstorm
508 disturbance, nutrient and soil moisture abundance, light harvesting competition) (Valladares et al., 2005a,b) that influ-
509 ence tree growth, and can therefore be leveraged to enhance predictions at the single tree level. The results showed a
510 consistently improved performance in tree diameter and AGB prediction when including context. The improvements
511 were tested as statistically significant in four of the six pairwise experiments, with size effect ranging from small to
512 large. Nevertheless, none of the morphometric variables obtained from the tree assemblage analysis proved useful to
513 improve predictions of tree-level DBH.

514 The Norway spruce forest under investigation exhibits a heterogeneous structure, with tree heights varying
515 markedly across space (Figure 5). Consequently, the UAV LiDAR survey produced a heterogeneous dataset (Da Silva
516 et al., 2006), a well-known challenge for automated tree phenotyping and functional trait mapping using ML meth-
517 ods (Schiefer et al., 2020). The accuracy enhancement gained from including context-aware features in the regression
518 experiments varied between the two datasets considered (i.e. SP-trees and CP-trees). Context-aware regressions of
519 DBH in SP-trees experienced greater enhancement than in CP-trees. This is consistent with the fact that the CP-
520 dataset contains less variability of context, since it is a locally clustered and more homogeneous dataset (Figure 2,
521 b). As SP-trees are grouped in scattered plots across the forest, their spatial distribution spans hundreds of meters,
522 making them subject to a more diverse context than the very local CP-dataset.

524 4.3 | The Role of Neighboring Context in Regression Performance

525 Most shallow learning methods achieved enhanced predictions when contextual information was included, with re-
526 sults consistently showing no deterioration (Tables 1 and 2), which indicates that even weak correlations could be
527 leveraged. The average heights of the 10 and 15 nearest neighbors were the most important context based predic-
528 tors for SP- and CP-trees, respectively (Figure 9). Moreover, neighboring tree heights were the most important and, to
529 a lesser extent, the LiDAR-based TWI, indicating that although TWI may be a good predictor of tree growth (Mohame-
530 dou et al., 2017), the neighborhood information resulted more useful, in agreement with previous literature (Ratcliffe
531 et al., 2015). In contrast, including features informing about neighbor dissimilarity, such as local outliers of tree height
532 detected using Local Outlier Factor (Breunig et al., 2000) and Isolation Forest (Liu et al., 2008) algorithms did not
533 result in enhanced predictions (thus not shown here). We hypothesize that metrics containing information about the
534 degree of local similarity may reveal the combined effect of ecological processes that are specific to the immediate
535 neighboring context. In contrast, metrics that proxy for dissimilarity do not help to uncover such processes, although
536 they remain useful in detecting outstanding trees (i.e. local outliers).

537 Context-based features at closer distances generally showed larger predictive power but also larger variance (as
538 less neighboring trees were computed). For instance, the p-value of Local Moran's I_i at a 20 m range in the CP-dataset
539 has an average positive effect but is not a stable predictor (Figure 9, a). This can be observed in the general trend
540 of larger standard deviations in the permutation importance of predictors retrieved at short ranges than at greater
541 distances (Annex VII). In accordance with competition-based studies (Lo and Lin, 2012; Sun et al., 2019; Zhang et al.,
542 2020), we observe that the strongest context-based predictors are those retrieved from the immediate neighboring
543 trees in both datasets, i.e. the average height of 5, 10 and 15 nearest neighbors. However, our method additionally
544 allows to compare the relative importance of competition-derived metrics and other context-based metrics operating
545 at larger scales. For instance, in Figure 9 (a) it is shown that local Moran's I_i retrieved at a 50 m range is compara-
546 ble in importance to the average height of the closest 10 neighboring trees. A general difference observed between
547 the CP and the SP-datasets is that the predictors' importances in the CP-dataset fluctuate more (i.e. larger standard
548 deviations). Further, in the SP-dataset, predictors rarely become negative and if they do, it is to a lesser extent. Mor-
549 phometric variables derived from tree assemblages (Figure 6) did not improve DBH predictions and were therefore
550 excluded from the final DBH models. Accordingly, assemblage-level morphometrics are not considered further as
551 predictive features. However, their consistent correlations with tree height were analysed separately to provide a
552 complementary insight into forest structure (Section 4.1).

554 Considering context metrics to enhance estimates of DBH at the individual tree level in coniferous forests has
555 been suggested in seminal works (Næsset, 1997; Næsset and Økland, 2002) and been adopted subsequently for var-
556 ious applications in forest research (Andersen et al., 2005; Rijal et al., 2012; Lo and Lin, 2012), finding information of
557 local context (e.g. canopy height) beneficial for estimation of e.g. wood volume and AGB components (Lim and Treitz,
558 2004; Kearsley et al., 2017; Sun et al., 2019). Moreover, recent investigations on tree morphology and productivity in
559 coniferous forests (Sun et al., 2019; Zhang et al., 2020) have motivated the further development of competition-aware
560 approaches to improve the prediction accuracy of individual tree traits (e.g. growth), leveraging tree canopy metrics.
561 In forest biomass research, a commonly recognized approach is calibrating regression models with plot-level metrics
562 for predicting tree-level structural traits (e.g. plot-level random effects in nonlinear mixed-effects methods), which has
563 been pointed out as a methodological limitation (Ratcliffe et al., 2015). Indeed, the results of such approaches are con-

strained by the artificially-delineated plot size, and it has been observed that accuracy increases with a progressively larger plot size (Hao et al., 2020; Liu et al., 2021). Our method to select context based on the spatial autocorrelation of tree heights (Figure 4) may indicate the range of saturation of such improvement (40 m in this study area). Furthermore, our results show that the variability and extent of context determines its beneficial leverage for prediction of tree-level traits (e.g. tree diameter, AGB).

59

This study continues this line of work and sheds light on how the local spatial context can be defined and leveraged in tree-level structural trait predictions (i.e. DBH), making a case for AGB estimates in a Norway spruce forest. The analysis shows that there is an optimal range to compute neighborhood metrics. In the study case considered here, this corresponded to a range including the closest 15 neighboring trees. Further, we found that the predictive power of context-based metrics is sensitive to context extent (i.e. the range at which such metrics are calculated). This observation may indicate that defining context based on plot-level metrics retrieved from artificially bounded units (Hao et al., 2020; Yang et al., 2020; Liu et al., 2021) may be seen as a constrained approach, as observed previously (Ratcliffe et al., 2015; Guillén-Escribà et al., 2021). Likewise, in light of this observation, and in line with recent studies (Zheng et al., 2022), determining the significant contextual extent of individual functional traits based on units of fixed size (e.g. pixel size) appears to be suboptimal. Therefore, future forest research would probably benefit from including context-awareness determined by spatial association of tree traits, bearing in mind that context-detection is trait-dependent and may vary depending on dataset source—e.g. spatial autocorrelation as a function of distance (Figure 4) is sensitive to CHM segmentation quality—and method applied—e.g. delineation of tree assemblages varied slightly between local Moran's I_i , and SL_i (Figure 5).

Lastly, we note that passive optical remote sensing studies usually define the optimal scale of analysis as a trade-off between the observational extent (i.e. area surveyed) and the image resolution (i.e. pixel size) (Ma et al., 2020; Zheng et al., 2022). Also, in ecological research, it is common to subsample datasets using natural subregions based on ancillary ecological criteria (e.g. ecoregions, conservation status) (Wang et al., 2019). Conversely, here we defined the range of influence of context-based metrics (i.e. the extent of tree neighborhoods) using a dataset-native approach, based entirely on the spatial association of individual tree heights. This permitted us to determine the context of influence unhampered by the remote sensing technique and not using external data sources. Furthermore, as local context was defined based on the spatial association of a real physical attribute (i.e. tree heights), and not defined by an artificially bounded unit (e.g. pixel size or plot size) the resulting distance could be considered characteristic of the forest ecosystem.

594 4.4 | Methods Applied and Limitations

We have aimed at preserving a fully-native UAV LiDAR approach, so that the applicability of the method proposed is not compromised by lacking local ancillary data (e.g. conservation status, edaphic conditions), whose availability may become a limiting factor in forest monitoring. We note that these findings are specific to the subalpine coniferous forest considered here. Caution is advised when contemplating a direct application of this approach to more complex canopy structures and terrains, such as those found in deciduous, multilayered or broadleaf forests—. Likewise, the strength of our results is currently limited by the lack of replicates at different forest sites, so that we cannot yet confirm these findings to be generally applicable to a wider range of forest types and canopy configurations. Furthermore, the pre-processing tasks (marked * in Figure 3, Section 2.3) required as part of our experimental design, simplifies the actual LiDAR scene representing the real forest scenario. This simplification hampers a fully-automated, streamlined application, and case-specific considerations are still required.

605 The workflow adopted here, including the required correction steps (Figure 3), highlights three key limitations: (i)
606 label assignment between field measurements and LiDAR-derived instances is imperfect; (ii) errors in individual tree
607 segmentation persist; and (iii) understory trees that are not detected by UAV LiDAR are consequently excluded from
608 the analysis. Imperfect label assignment (i) prevents a robust and automated one-to-one correspondence between
609 measured DBH and LiDAR-derived tree height, even in this structurally simple forest. Small stem inclinations, for
610 example, can result in crown displacements of several meters for average-height trees. Such effects are expected to
611 become more pronounced in structurally complex or multilayered canopies. Segmentation errors (ii) primarily result
612 in omission errors, such as multiple real trees being represented as a single LiDAR segment, which complicates label
613 matching. In contrast, preliminary tests conducted in a broadleaf forest (Laegeren Forest Site) using the same param-
614 eterisation revealed a high prevalence of commission errors, where individual branches were incorrectly segmented
615 as separate trees. The shift between the field-based inventory tree datasets and the UAV-LiDAR datasets (Figure 14,
616 panels a and b, respectively, in Annex V) shows a clear thinning, particularly at the lower end of tree heights (which
617 usually correspond to understory trees). As a result, the distribution densities of CP- and SP-datasets captured by
618 the UAV LiDAR system, show a drift towards higher tree tops and broader stems, as the top canopy is what is being
619 predominantly portrayed in the LiDAR scene.

620 These corrections may have influenced the derived context-based features, and future work could assess whether
621 such predictors are also effective in inventory-based datasets. Nevertheless, studies using competition-based metrics
622 (Lo and Lin, 2012; Sun et al., 2019; Zhang et al., 2020) and nonlinear mixed-effects methods (Hao et al., 2020; Yang
623 et al., 2020; Liu et al., 2021) indicate that the contextual information derived from plot-level metrics is informative.
624 Here, we aimed to translate these approaches into a framework native to UAV LiDAR data, where context is not
625 constrained by artificially delineated plot boundaries, albeit at the cost of limited understory representation. A natural
626 extension of this workflow would integrate terrestrial laser scanning with the UAV LiDAR survey to address this
627 limitation.

628 5 | CONCLUSIONS

629 This study introduces an integrated UAV LiDAR framework that first characterises forest structure, through an eco-
630 logical assessment of gradients of tree heights and tree assemblage morphology, and subsequently applies context-
631 aware modelling to improve estimates of tree diameter and derived aboveground biomass in a coniferous forest. The
632 prediction performance demonstrated improvements in tree diameter and aboveground biomass prediction when in-
633 corporating context-aware features—the exception was the Lasso regression, which stagnated in one of the datasets
634 considered (SP-dataset)—and in no case did contextual features have a detrimental effect. The results show that the
635 use of context-aware features as predicting variables can improve estimates of tree diameter and thus have substan-
636 tial impact on aboveground biomass estimates in coniferous forests. The best performing model showed a reduction
637 of RMSE in tree diameter predictions of 4.1% and 0.8% in the sparse (i.e. SP) and in the continuous (i.e. CP) dataset,
638 respectively, which suggests that an heterogeneous forest context supported the regression improvements. For the
639 best performing method (AdaBoost regression), the strongest context-based predictors were the average heights of
640 the nearest 5–15 neighboring trees. Features that provide information about the tree neighborhood (e.g. spatial lag
641 of tree height, average height of k-nearest trees) contain useful information (i.e. weak but consistent correlations)
642 which can be leveraged by shallow learning methods to improve predictions of diameter at breast height, and above-
643 ground biomass. In contrast, adding morphometric variables from the tree assemblages as predictors did not enhance
644 tree diameter prediction accuracy. This finding suggests that the information retrieved from the local context serves

645 as a proxy for underlying ecological mechanisms that exert influence on the individual tree diameter and therefore
646 aboveground biomass, as a result of local adaptations to microclimate, edaphic conditions and biotic factors. We con-
647 clude that the use of UAV LiDAR surveys and the integration of the spatial associations of tree heights is an efficient
648 approach to incorporate context and thus enhance forest biomass surveying.

649 Author contributions

650 **Original conceptual framework:** Jaime C. Revenga and Stefan Oehmcke; **experimental design:** Jaime C. Revenga;
651 **UAV–LiDAR data collection:** Jaime C. Revenga; **field-based data provision and curation:** Flurin Sutter and Mana
652 Gharun; **laser data pre- and postprocessing:** Jaime C. Revenga; **feature engineering, training and evaluation of the ma-**
653 **chine learning models:** Jaime C. Revenga and Stefan Oehmcke; **visualisation:** Jaime C. Revenga; **supervision:** Alexan-
654 der Damm, Katerina Trepekli and Fabian Gieseke; **project administration:** Jaime C. Revenga, Alexander Damm, Nina
655 Buchmann, Katerina Trepekli, Fabian Gieseke; **writing—original draft preparation:** Jaime C. Revenga; **writing—review**
656 **and editing:** Stefan Oehmcke, Mana Gharun, Flurin Sutter, Fabian Gieseke, KT, NB, Alexander Damm and Jaime C.
657 Revenga. All authors have read and agreed to the published version of the manuscript.

658 Acknowledgements

659 Helpful discussions with Thomas Friberg, Daniel Kükenbrink and Moritz Bruggisser are gratefully acknowledged. Like-
660 wise, we acknowledge the contribution of the field workers, who are responsible for collecting the forest inventory
661 data on a regular basis, used here as ground truth.

662 Conflicts of Interest

663 The authors declare that they have no known competing financial interests or personal relationships that could have
664 appeared to influence the work reported in this paper.

665 Funding

666 This project received funding support from the Talent Program Horizon 2020/Marie Skłodowska-Curie Actions, a
667 Villum Experiment grant by the Velux Foundations, DK (MapCland project, number: 00028314), and the DeepCrop
668 project (UCPH Strategic plan 2023 Data + Pool). Mana Gharun also acknowledges funding by Swiss National Science
669 Foundation project ICOS-CH Phase 3 (20F120_1982287).

670 Data Availability

671 The code, data and metadata that support the findings of this study are available from the corresponding author,
672 JCR, upon responsible request, and will be published in a DOI-compliant public repository upon acceptance of this
673 manuscript.

674 Supporting Information

675 | Annex I: Context Detection

676 The distance range selected around each tree to compute neighborhood metrics (i.e. context detection), was con-
 677 ducted based on the peak of significance (determined using the standard z-score) of local spatial autocorrelation
 678 (using Local Moran's I_i) as function of increasing distance, in steps of 10 m.

679

680 Local Moran's I_i is a spatial statistic that relates attribute similarity to locational similarity, mapping the autocorre-
 681 lation of individual tree heights across the geographical space, as defined above (Eq. 1, in Section 3.1). The expression
 682 below (Eq. 6) defines the z-score, which is used to measure the significance of tree-height clustering. Z-scores shows
 683 the significance of the clustering by subtracting the observed I_i values from the expectation (i.e. $E[I_i]$), and normal-
 684 izing over the standard deviation of I_i . This produces a distance metric in units of standard deviations. $E[I_i]$ is the
 685 expected value of local Moran's I_i under the null hypothesis of no spatial autocorrelation.

$$686 z_{score} = \frac{I_i - E[I_i]}{\sqrt{V[I_i]}}, \quad (6)$$

686 Neighborhood size was determined according to the significance of spatial autocorrelation (defined as local Moran's
 687 I_i) as function of distance, via the standard z-score. The expected value of Moran's I under the null hypothesis of no
 688 spatial autocorrelation is:

$$689 E[I_i] = -\frac{\sum_{j=1}^m w_{i,j}}{m-1} = -\frac{1}{m-1} \quad (7)$$

689 where m equals the total number of trees in the neighborhood. At large sample sizes (i.e. for increasing values
 690 of m), the expected value approaches zero. The spatial weights allocated to each neighboring tree j are standard-
 691 ized (Anselin et al., 2001), such that for each tree i , $\sum_j w_{i,j} = 1$. Finally, the variance of local Moran's I_i is defined as
 692 the expectation of the square of I_i , minus the square of the expectations of I_i :

$$693 V[I_i] = E[I^2] - E[I_i]^2 \quad (8)$$

693 | Annex II: Preprocessing Tasks

694 To guarantee that only the trees detected by LiDAR were included in the regression analysis, a pre-processing step
 695 was necessary (marked * in Figure 3). First, understory trees that passed unnoticed to the UAV LiDAR survey were
 696 removed. Second, we filtered clumped trees by selecting the field-based measurement of the highest tree when
 697 two ground measurements were less than 1 m apart, while removing the measurement of the shorter tree. Third,
 698 we corrected for a crown shift effect, i.e. some high and skewed trees were affected by the presence of a smaller
 699 neighboring tree (affecting less than 5% of the trees) being closer to its corresponding individual tree crown polygon
 700 centroid, thus introducing a wrongly allocated label between the field-based measurement and the LiDAR-derived
 701 metrics. The resulting distribution is shown in Figure 14b.

702 A second data preparation step was executed prior to the morphometric analysis of tree assemblages. (marked

703 ** in Figure 3). First, single tree crown polygons were merged based on either local Moran's I_i ([Anselin, 1995](#)) or
704 SL_i ([Anselin et al., 2009](#)) (Section 2.3). These new larger polygons describe the two-dimensional projection of tree
705 assemblages. Then, as our interest focused on the extent and shape of the tree assemblages, the inner borders of the
706 merged polygons were discarded. To reduce computation time, the polygon shapes were simplified by reducing the
707 number of vertices and edges to 70% while keeping the polygon shape.

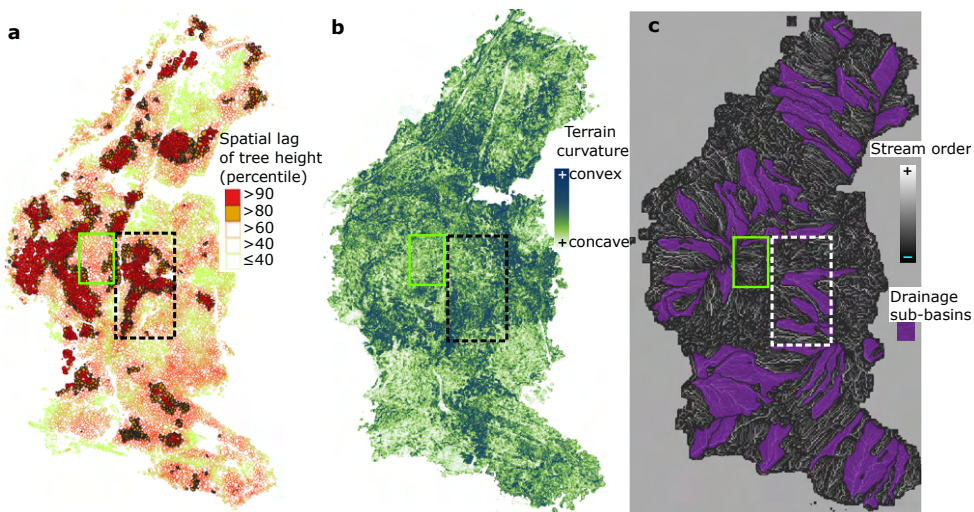


FIGURE 10 a: Spatial lag of tree height derived from the individual tree crown polygon dataset. b: Map of terrain curvature derived from LiDAR ground-returns. c: Hydrological network (Strahler's stream order) (Strahler, 1952). In all three panels, the dashed box indicates an area favored by surface hydrological conditions, hosting an assemblage of trees in the >90 % percentile of spatial lag of tree height. The solid green box indicates an area at a hilltop, unfavored by surface hydrological processes, more exposed to windstorm disturbance, and hosting an assemblage of trees in the < 60% percentile of spatial lag of tree height.

708 | Annex III: Morphometry of Tree Assemblages

709 In the coniferous forest site considered in this study, the spatial distribution of SL_i of tree heights presents directional
 710 anisotropy, stretching across preferential areas which seem to match sheltered sectors of the forest, such as concave
 711 thalwegs. Figure 10 highlights two neighboring areas with contrasting values of SL_i , which may indicate that surface
 712 hydrology processes and terrain exposure (i.e. terrain convexity) condition tree growth at the group level. No manage-
 713 ment activities or harvesting have occurred in the study area, apart from a 2005 clearing event that partially affected
 714 SP-6. Consequently, the forest structure can be considered shaped primarily by natural abiotic and biotic factors.

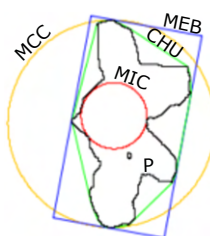


FIGURE 11 Calculation of elementary geometries fitted to an exemplary tree assemblage. P: polygon of tree assemblage (black line). MCC: minimum circumscribed circle (in green). MIC: maximum inscribed circle (in red). CHU: convex hull (in yellow). MEB: minimum enclosing box containing P (in blue).

715 The morphometric analysis was conducted by taking into account the outer borders of tree assemblages defined

716 either by SL_i , or by local Moran's I_i (delineated as explained in Section 2.3; results shown in Figure 5). The 20 basic
 717 morphometric variables (Table 3) result from fitting elementary geometries to the tree assemblage polygon. The 20
 718 derived variables (Table 4) are adimensional parameters (except for concavity, in m^2) obtained by combining the basic
 719 parameters.

TABLE 3 Twenty basic morphometric variables derived from the tree assemblage polygon dataset (as described in Güler et al., 2021) (Güler et al., 2021). P: polygon of a tree assemblage.

Basic parameters	Description	units
XPOL	Easting of P centroid	m
YPOL	Northing of P centroid	m
APOL	Area of P	m^2
PPOL	Perimeter of P	m
LPOL	Major axis' length of P	m
WPOL	Minor axis' length of P	m
N-S	North-South alignment of P, defined as $ \sin(\text{azimuth}) $ of major axis	ϕ
ABOB	Area of the bounding box fully containing P	m^2
PBOB	Perimeter of the bounding box fully containing P	m
AMEB	Area of minimum enclosing box	m^2
PMEB	Perimeter of minimum enclosing box	m
ACHU	Area of the convex hull fully containing P	m^2
PCHU	Perimeter of the convex hull fully containing P	m
AMCC	Area of the minimum circumscribed circle enclosing P	m^2
PMCC	Perimeter of the minimum circumscribed circle enclosing P	m
RMCC	Radius of the minimum circumscribed circle enclosing P	m
AMIC	Area of the maximum inscribed circle enclosing P	m^2
PMIC	Perimeter of the maximum inscribed circle enclosing P	m
RMIC	Radius of the maximum inscribed circle enclosing P	m

720 In Figure 12 we show the morphometric variables, obtained from the delineated tree assemblages, that showed
 721 the highest correlation with spatial lag of tree heights.

TABLE 4 20 morphometric variables derived from the tree assemblage polygon dataset (as described in (Güler et al., 2021)). P: tree assemblage polygon. A: area of P. L: length of major axis of P. W: width of minor axis of P (i.e. width). ACHU: area of convex hull fully containing P. RMCC: radius of minimum circumscribed circle. PCHU: perimeter of convex hull fully containing P. AMEB: area of minimum enclosing box.

Derived parameters	Name	Definition	Source
LTWR	Length-to-width ratio	L/W	(Horton, 1932)
WTLR	Width-to-Length ratio	W/L	(Zingg, 1935)
ELLF	Ellipticity Factor	$ L - W /(L + W)$	(Buendia et al., 2002)
CIRR	Circularity Ratio	P^2/A	(Attnave and Arnoult, 1956)
ZFOR	Zăvoianu's Form Factor	$(16A)/P^2$	(Zăvoianu, 1978)
COMF	Compactness Factor	$P/(4\pi A)^{0.5}$	(Güler et al., 2021)
MCIR	Miller's Circularity Ratio	$(4\pi A)/P^2$	(Miller, 1953)
DISM	Dispersion Measure	$1 - [(4\pi A)^{0.5}/P]$	(Attnave and Arnoult, 1956)
COMI	Complexity Index	$1 - [(4\pi A)/P^2]$	(Güler et al., 2021)
HFOR	Horton's Form Factor	A/L^2	(Horton, 1932)
ELOF	Elongation Factor	$(4A/\pi)^{0.5}/L$	(Schumm, 1956)
LEMR	Lemniscate Ratio	$(\pi L^2)/4A$	(Chorley et al., 1957)
REGF	Regularity Factor	$(\pi LW)/4A$	(Buendia et al., 2002)
SHAF	Shape Factor	$[(4\pi A)/P^2] \times (L/W)$	(Buendia et al., 2002)
CONV	Convexity	$PCHU/P$	(Horgan and Glasbey, 1995)
CONC	Concavity	$ACHU - A$	(Landini, 2010)
SOLI	Solidity	$A/ACHU$	(Zunic and Rosin, 2004)
RECT	Rectangularity	$A/AMEB$	(Rosin, 1999)
ROUN	Roundness	$(4\pi A)/(PCHU)^2$	(Horgan and Glasbey, 1995)
SPHE	Sphericity	$(4A/\pi)^{0.5}/(2 \times RMCC)$	(Wadell, 1935)

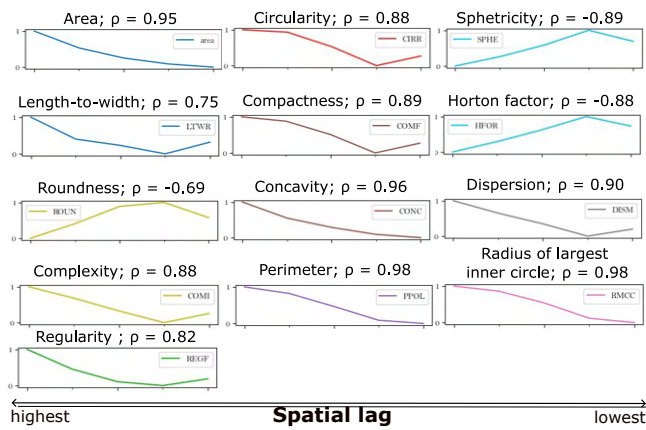


FIGURE 12 Correlation coefficients between (i) the most prominent morphometric variables derived from tree assemblages and (ii) spatial lag. The five ticks on the x-axis correspond to assemblage groups ordered from high to low spatial lag (left to right).

724 | Annex IV: Training, Validation and Test of results

725 Nested cross-validation (NCV) ([Bates et al., 2021](#)) follows the updated and established recommendations to achieve
 726 an unbiased estimate of the generalization error, while making optimal use of the limited available data. It is an
 727 evaluation method for determining the accuracy of point estimates and confidence intervals for prediction errors.
 728 As a modification developed from standard cross-validation ([Berrar, 2018](#)), NCV improves estimates of prediction
 729 accuracy and confidence intervals by accounting for the correlation between error estimates in different folds, an
 730 inconvenient phenomenon affecting standard cross-validation that may render error estimates overly optimistic. How
 731 NCV is implemented is shown in Figure 13. The entire algorithmic routine of NCV is presented immediately below.
 732 The input data (i.e. X,Y) corresponds to the set of predictors (i.e. X), and the target variable DBH (i.e. Y), respectively.

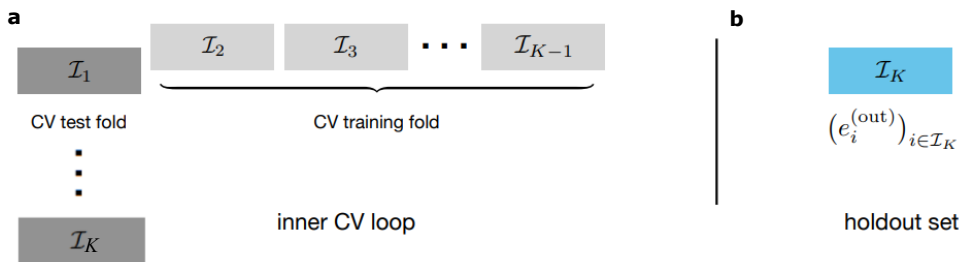


FIGURE 13 Visualization of 10-fold nested cross-validation (CV). **a:** at each of the K steps ($K = 10$), we perform standard cross-validation for model training (light grey folds), holding one of the folds out of the inner CV loop (dark grey fold). **b:** The fresh holdout folds (in blue) are never used for hyperparameter optimization or feature selection (figure adapted from Bates et al., 2021 ([Bates et al., 2021](#))).

Algorithm 1: Nested cross-validation

Input: data (X, Y) , fitting algorithm A , loss ℓ , number of folds K , number of repetitions R

procedure Nested cross-validation (X, Y) // \triangleright primary algorithm;

```

 $es \leftarrow []$  //  $\triangleright$  initialize empty vectors;
 $a\_list \leftarrow []$  //  $\triangleright$  (a) terms;
 $b\_list \leftarrow []$  //  $\triangleright$  (b) terms;
for  $r \in \{1, \dots, R\}$  do
    Randomly assign points to folds  $I_1, \dots, I_K$ ;
    for  $k \in \{1, \dots, K\}$  do
        //  $\triangleright$  outer CV loop;
         $e^{(in)} \leftarrow$  inner cross-validation( $X, Y, \{I_1, \dots, I_K\} \setminus I_k$ ) //  $\triangleright$  inner CV loop;
         $\hat{\theta} \leftarrow A((X_i, Y_i)_{i \in I \setminus I_k})$ ;
         $e^{(out)} \leftarrow (\ell(\hat{f}(X_i, \hat{\theta}), Y_i))_{i \in I_k}$ ;
         $a\_list \leftarrow$  append( $a\_list, (mean(e^{(in)}) - mean(e^{(out)}))^2$ );
         $b\_list \leftarrow$  append( $b\_list, var(e^{(out)}) / |I_k|$ );
         $es \leftarrow$  append( $es, e^{(in)}$ )
    
```

 $\widehat{MSE} \leftarrow mean(a_list) - mean(b_list)$;
 $\widehat{Err}^{(NCV)} \leftarrow mean(es)$;
return: $(\widehat{Err}^{(NCV)}, \widehat{MSE})$ // \triangleright prediction error estimate and MSE estimate;

procedure Inner cross-validation $(X, Y, \{I_1, \dots, I_{K-1}\})$ // \triangleright inner cross-validation subroutine;

```

 $e^{(in)} \leftarrow []$ ;
for  $k \in \{1, \dots, K-1\}$  do
     $\hat{\theta} \leftarrow A((X_i, Y_i)_{i \in I_i \cup \dots \cup I_{K-1} \setminus I_k})$ ;
     $e^{(temp)} \leftarrow (\ell(\hat{f}(X_i, \hat{\theta}), Y_i))_{i \in I_k}$ ;
     $e^{(in)} \leftarrow$  append( $e^{(in)}, e^{(temp)}$ );
return:  $e^{(in)}$  ;

```

Output: Nested cross-validation (X, Y)

733 | Annex V: Distribution Shift Between CP-trees and SP-trees

734 Here below, we show the joint distributions of DBH and tree height in the two datasets considered (SP-trees, CP-
 735 trees) in order to highlight how differently distributed they are—both in field-based inventory (Figure 14a) and in the
 736 dataset captured by the UAV LiDAR system (Figure 14b). The joint distributions of DBH and tree height in both CP and
 737 SP-datasets show a shift between the two ([Quionero-Candela et al., 2009](#)), which justifies treating them separately.
 738 The kernel probability distribution of heights shows that the SP-dataset contains a higher amount of short trees (i.e.
 739 3-10 m), which cover a wide range of DBH values (i.e. 5-20 cm). Also, the range of DBH is broader in the SP-dataset
 740 compared to the CP-dataset, and the SP-instances do not exhibit an accumulation in the center as evident as the one
 741 observed in the CP-dataset.

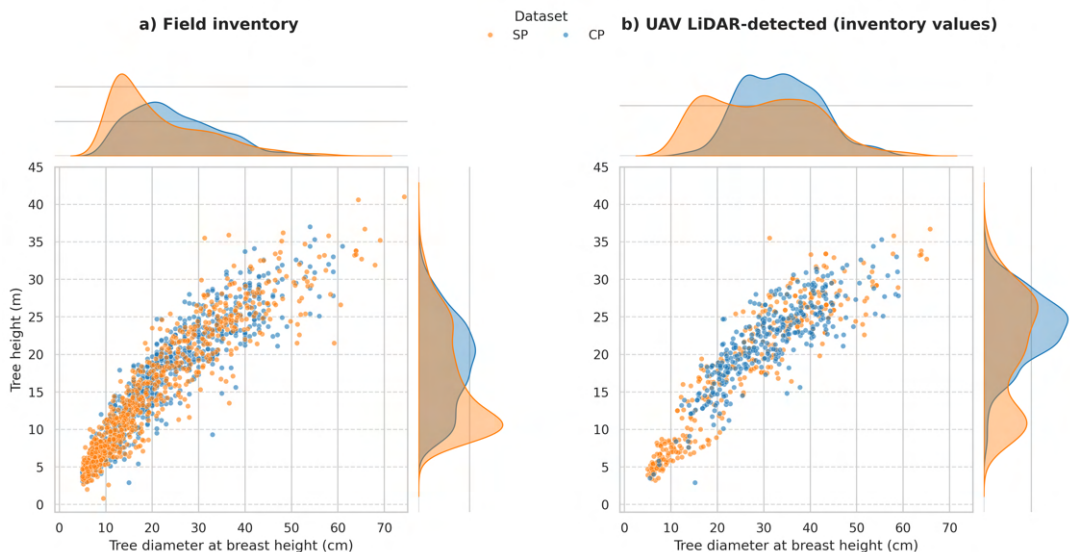


FIGURE 14 Joint distributions of diameter at breast-height and tree height from field-based inventory data. a: Field inventory; b: trees in field inventory detected by the UAV LiDAR system. It should be noted that the two datasets (i.e. SP-trees, CP-trees) are differently distributed—i.e. there is a shift ([Quionero-Candela et al., 2009](#)) between Sparse Measurement Plots (SP) and Continuous Measurement Plots (CP) datasets.

742 | Annex VI: Elevation Map of the Study Site and Location of SP-plots

743 We provide the digital elevation model of the study area (Figure 15, a) to understand differences in flight heights
 744 (Figure 2) and to complement the information given on terrain exposure and surface hydrology (Figure 10). Figure 15,
 745 (b) shows the five rejected SP-plots and one valid (i.e. SP-18), for comparison. Among the rejected SP-plots, 1, 2, 9 and
 746 10 show an insufficiently descriptive CHM, while SP-14 shows an intractable allocation of ground-based labels. All
 747 five rejected SP-plots were discarded before starting the modelling process, so they did not take part in the regression
 748 experiments.

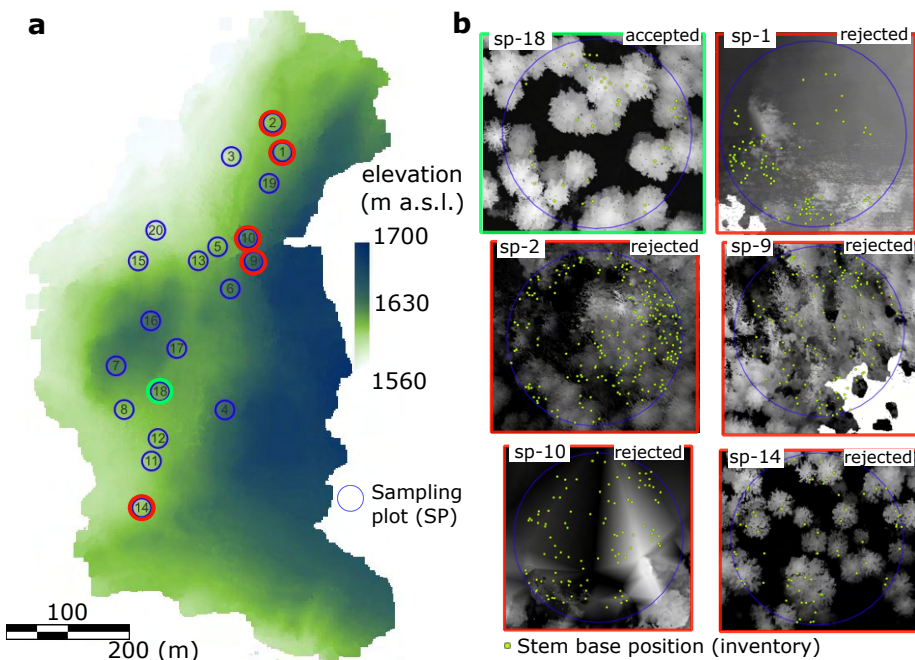


FIGURE 15 a: Digital elevation model of the study area. a.s.l.: elevation above sea level, in m. The blue circles represent the SP-plots, numbered by their ID code (1-20). The green and red circles refer to the plots shown in panel b. b: Five SP-plots rejected and one valid (SP-18) given for comparison of contrasting quality of canopy height models, derived from the UAV LiDAR point cloud data. In all six SP-plots, the yellow dots indicate the location of tree stems according to the field-based inventory.

749 | Annex VII: Importance of predictors considered

750 Figure 16 shows the importance of all predictors initially considered (41) in the context-aware regression experiment.
751 Results show the permutation importances for the best performing model (i.e. AdaBoost) in both datasets (CP-dataset
752 and SP-dataset).

753

754 Besides tree-level and context-based predictors, we included topographic wetness index (TWI) as a predictor,
755 which is a well-established environmental factor determining favorable hydrological conditions for tree growth. TWI
756 is a steady state wetness index used to evaluate topography-dependent surface hydrology processes. According to
757 the established definition ([Beven and Kirkby, 1979](#)), TWI is calculated as $\frac{a}{\tan(b)}$, where a represents the upslope area
758 draining through the point of interest, and b indicates the local slope. The parameterization considered to calculate
759 TWI followed the suggestions of Kopecký et al. (2021) ([Kopecký et al., 2021](#)) for soil moisture estimation. In order
760 to discern how much the contribution of TWI is influenced by granularity, we calculated it at a 2 m, 5 m and 10 m
761 resolution, and included it as separate predictors.

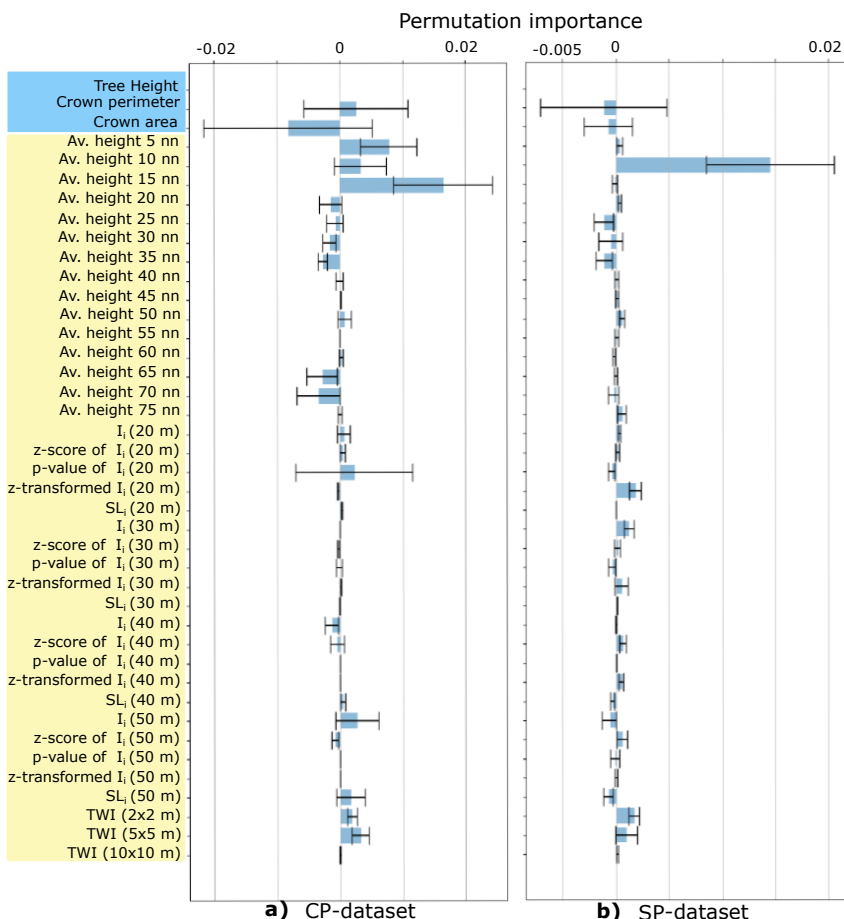


FIGURE 16 Inspection of predictors' importance via the permutation method (Altmann et al., 2010) in the Adaboost regression experiment in context-aware conditions. The left panel (a) shows results in the Continuous Measurement Plot (CP) dataset, and the right panel (b) shows results in the Sparse Measurement Plot (SP) dataset. Bar length and error bar show the mean and standard deviation of a predictor's importance, respectively. A negative mean value indicates that a predictor is less useful than when being randomly shuffled, so it lowers the model's predictive performance. Predictors highlighted in blue are individual tree traits; predictors highlighted in yellow are context-based (i.e. either neighborhood metrics or topographic wetness index, TWI). In both datasets, it can be noted how the average heights of the nearest 5–15 neighbors (nn) stand out as the strongest predictors, outperforming crown perimeter and crown area. In both plots (a and b), individual tree height (with importance: 0.85 in CP-dataset; 1.3 in SP-dataset) has been removed to facilitate visual comparison of the remaining predictors.

763 Graphical Abstract

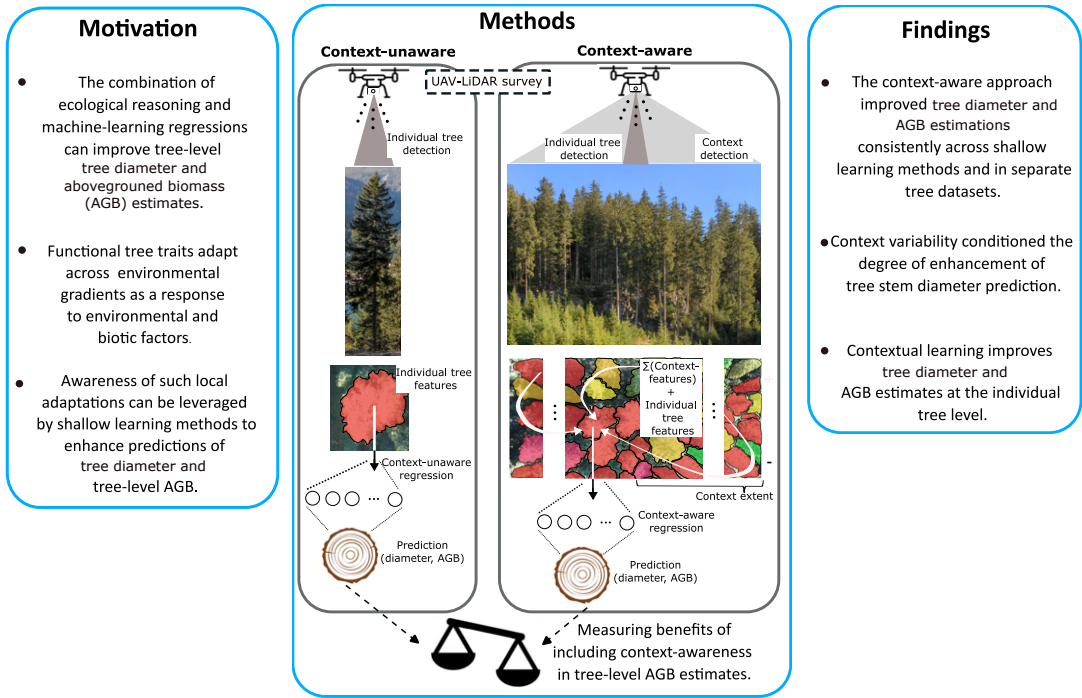


FIGURE 17 Graphical Abstract of the study.

764 References

- Altmann, A., Tološi, L., Sander, O. and Lengauer, T. (2010) Permutation importance: a corrected feature importance measure. *Bioinformatics*, **26**, 1340–1347.
- Andersen, H.-E., McGaughey, R. J. and Reutebuch, S. E. (2005) Estimating forest canopy fuel parameters using lidar data. *Remote sensing of Environment*, **94**, 441–449.
- Anselin, L. (1995) Local indicators of spatial association—lisa. *Geographical analysis*, **27**, 93–115.
- Anselin, L. and Rey, S. J. (2010) Perspectives on spatial data analysis. In *Perspectives on spatial data analysis*, 1–20. Springer.
- Anselin, L., Syabri, I. and Kho, Y. (2009) Geoda: an introduction to spatial data analysis. In *Handbook of applied spatial analysis: Software tools, methods and applications*, 73–89. Springer.
- Anselin, L. et al. (2001) Spatial econometrics. *A companion to theoretical econometrics*, **310330**.
- Antonio, N., Tome, M., Tome, J., Soares, P. and Fontes, L. (2007) Effect of tree, stand, and site variables on the allometry of eucalyptus globulus tree biomass. *Canadian Journal of Forest Research*, **37**, 895–906.
- Attneave, F. and Arnoult, M. D. (1956) The quantitative study of shape and pattern perception. *Psychological bulletin*, **53**, 452.

- 777 Baccini, A., Walker, W., Carvalho, L., Farina, M., Sulla-Menashe, D. and Houghton, R. (2017) Tropical forests are a net carbon
778 source based on aboveground measurements of gain and loss. *Science*, **358**, 230–234.
- 779 Bates, S., Hastie, T. and Tibshirani, R. (2021) Cross-validation: what does it estimate and how well does it do it? *arXiv preprint*
780 *arXiv:2104.00673*.
- 781 Berrar, D. (2018) Cross-validation. *Encyclopedia of Bioinformatics and Computational Biology*, **1**, 542–545.
- 782 Berntsen, M. D. and Callaway, R. (1994) Positive interactions in communities. *Trends in ecology & evolution*, **9**, 191–193.
- 783 Beven, K. J. and Kirkby, M. J. (1979) A physically based, variable contributing area model of basin hydrology/un modèle à base
784 physique de zone d'appel variable de l'hydrologie du bassin versant. *Hydrological sciences journal*, **24**, 43–69.
- 785 Biging, G. S. and Dobbertin, M. (1995) Evaluation of competition indices in individual tree growth models. *Forest science*, **41**,
786 360–377.
- 787 Breunig, M. M., Kriegel, H.-P., Ng, R. T. and Sander, J. (2000) Lof: identifying density-based local outliers. In *Proceedings of the*
788 *2000 ACM SIGMOD international conference on Management of data*, 93–104.
- 789 Buendia, P., Soler, C., Paolicchi, F., Gago, G., Urquieta, B., Pérez-Sánchez, F. and Bustos-Obregón, E. (2002) Morphometric-
790 characterization and classification of alpaca sperm heads using the sperm-class analyzer® computer-assisted system.
791 *Theriogenology*, **57**, 1207–1218.
- 792 Burri, S. (2019) Long-term environmental research—the davos-seehornwald site. URL: <https://doi.org/10.3929/ethz-b-000328277>.
- 794 Cabo, C., Ordóñez, C., López-Sánchez, C. A. and Armesto, J. (2018) Automatic dendrometry: Tree detection, tree height and
795 diameter estimation using terrestrial laser scanning. *International journal of applied earth observation and geoinformation*,
796 **69**, 164–174.
- 797 Chen, Q., Baldocchi, D., Gong, P. and Kelly, M. (2006) Isolating individual trees in a savanna woodland using small footprint
798 lidar data. In *Photogrammetric Engineering and Remote Sensing*, 72(8): 923–932, 923–932.
- 799 Chorley, R. J., Malm, Donald E., E. and Pogorzelski, H. A. (1957) A new standard for estimating drainage basin shape. *American*
800 *Journal of Science*, **255**, 138–141.
- 801 Chu, H.-J., Wu, C.-F. and Lin, Y.-P. (2013) Incorporating spatial autocorrelation with neural networks in empirical land-use
802 change models. *Environment and Planning B: Planning and Design*, **40**, 384–404.
- 803 Cliff, N. (1993) Dominance statistics: Ordinal analyses to answer ordinal questions. *Psychological bulletin*, **114**, 494.
- 804 Cressie, N. (2015) *Statistics for spatial data*. John Wiley & Sons.
- 805 Da Silva, B. C., Basso, E. W., Bazzan, A. L. and Engel, P. M. (2006) Dealing with non-stationary environments using context
806 detection. In *Proceedings of the 23rd international conference on Machine learning*, 217–224.
- 807 Dalponte, M. and Coomes, D. A. (2016) Tree-centric mapping of forest carbon density from airborne laser scanning and
808 hyperspectral data. *Methods in ecology and evolution*, **7**, 1236–1245.
- 809 Davidson, L., Mills, J., Haynes, I., Augarde, C., Bryan, P. and Douglas, M. (2019) Airborne to uas lidar: An analysis of uas lidar
810 ground control targets. *ISPRS Geospatial Week*.
- 811 Duncanson, L., Armston, J., Disney, M., Avitabile, V., Barbier, N., Calders, K., Carter, S., Chave, J., Herold, M., Crowther, T. W.
812 et al. (2019) The importance of consistent global forest aboveground biomass product validation. *Surveys in geophysics*,
813 **40**, 979–999.
- 814 ESRI (2021) ArcGis Pro: Implementation Guide. Redlands, California. URL: www.esri.com.

- 815 Fatichi, S., Pappas, C., Zscheischler, J. and Leuzinger, S. (2019) Modelling carbon sources and sinks in terrestrial vegetation.
816 *New Phytologist*, **221**, 652–668.
- 817 Freund, Y. and Schapire, R. E. (1997) A decision-theoretic generalization of on-line learning and an application to boosting.
818 *Journal of computer and system sciences*, **55**, 119–139.
- 819 Friedlingstein, P., Jones, M. W., O'sullivan, M., Andrew, R. M., Hauck, J., Peters, G. P., Peters, W., Pongratz, J., Sitch, S., Le Quéré,
820 C. et al. (2019) Global carbon budget 2019. *Earth System Science Data*, **11**, 1783–1838.
- 821 Friedman, J. H. (2001) Greedy function approximation: a gradient boosting machine. *Annals of statistics*, 1189–1232.
- 822 Getis, A. and Ord, J. K. (2010) The analysis of spatial association by use of distance statistics. In *Perspectives on spatial data
analysis*, 127–145. Springer.
- 823 Gielen, B., Acosta, M., Altimir, N., Buchmann, N., Cescatti, A., Ceschia, E., Fleck, S., Hortnagel, L., Klumpp, K., Kolari, P. et al.
824 (2018) Ancillary vegetation measurements at icos ecosystem stations. *International Agrophysics*, **32**, 645–664.
- 825 Goebes, P., Schmidt, K., Seitz, S., Both, S., Bruehlheide, H., Erfmeier, A., Scholten, T. and Kühn, P. (2019) The strength of
826 soil-plant interactions under forest is related to a critical soil depth. *Scientific Reports*, **9**, 8635.
- 827 Green, J. K. and Keenan, T. F. (2022) The limits of forest carbon sequestration. *Science*, **376**, 692–693.
- 828 Gryc, V. and Horáček, P. (2007) Variability in density of spruce (*picea abies* [L.] karst.) wood with the presence of reaction
829 wood. *Journal of forest science*, **53**, 129–137.
- 830 Guillén-Escribà, C., Schneider, F. D., Schmid, B., Tedder, A., Morsdorf, F., Furrer, R., Hueni, A., Niklaus, P. A. and Schaeppman,
831 M. E. (2021) Remotely sensed between-individual functional trait variation in a temperate forest. *Ecology and Evolution*,
832 **11**, 10834–10867.
- 833 Güler, C., Beyhan, B. and Tağa, H. (2021) Polymorph-2d: An open-source gis plug-in for morphometric analysis of vector-based
834 2d polygon features. *Geomorphology*, **386**, 107755.
- 835 Gundersen, P., Thybring, E. E., Nord-Larsen, T., Vesterdal, L., Nadelhoffer, K. J. and Johannsen, V. K. (2021) Old-growth forest
836 carbon sinks overestimated. *Nature*, **591**, E21–E23.
- 837 Hao, Y., Widagdo, F. R. A., Liu, X., Quan, Y., Dong, L. and Li, F. (2020) Individual tree diameter estimation in small-scale forest
838 inventory using uav laser scanning. *Remote Sensing*, **13**, 24.
- 839 Heiskanen, J., C., B., N., B., C., C., H., C., B., G., T., G., S., H., S., H., M., H., I.A., J., A., J., E., J., U., K., V., K., B., K., I., L. H. L., M.-L.,
840 L., D., L., L., M., C., L. M., D., P., M., P., K., P., M., R., C., R., J., R., L., R., E., S., R., S., M., S., T., S., A., W., A.T., V., T., V., G.,
841 V. and W., K. (2022) The integrated carbon observation system in europe. *Bulletin of the American Meteorological Society*,
842 **103**, E855–E872.
- 843 Ho, T. K. (1995) Random decision forests. In *Proceedings of 3rd international conference on document analysis and recognition*,
844 vol. 1, 278–282. IEEE.
- 845 Horgan, G. W. and Glasbey, C. A. (1995) Uses of digital image analysis in electrophoresis. *Electrophoresis*, **16**, 298–305.
- 846 Horton, R. E. (1932) Drainage-basin characteristics. *Transactions, American geophysical union*, **13**, 350–361.
- 847 Hyypä, E., Yu, X., Kaartinen, H., Hakala, T., Kukko, A., Vastaranta, M. and Hyypä, J. (2020) Comparison of backpack, hand-
848 held, under-canopy uav, and above-canopy uav laser scanning for field reference data collection in boreal forests. *Remote
849 Sensing*, **12**, 3327.
- 850 ICOS, . (2026) Icos-ch ecosystem station davos. <https://www.icos-switzerland.ch/davos>. Accessed: 2026-01-19.
- 851 ICOS (2008) Integrated carbon observation system. URL: <https://www.icos-cp.eu/>. Accessed: 2023-02-04.

- 853 — (2019) Icos handbook 2019. Technical report, Integrated Carbon Observation System (ICOS) Research Infrastructure. URL:
854 https://www.icos-cp.eu/sites/default/files/2019-05/ICOS_handbook_2019.pdf.
- 855 ICP Forests (1985) International co-operative programme on assessment and monitoring of air pollution effects on forests.
856 URL: <http://icp-forests.net/>. Accessed: 2023-02-04.
- 857 Jafari, F., Moradi, K. and Shafiee, Q. (2024) Shallow learning vs. deep learning in engineering applications. In *Shallow Learning
858 vs. Deep Learning: A Practical Guide for Machine Learning Solutions*, 29–76. Springer.
- 859 Kearsley, E., Moonen, P. C., Hufkens, K., Doetterl, S., Lisingo, J., Boyemba Bosela, F., Boeckx, P., Beeckman, H. and Verbeeck,
860 H. (2017) Model performance of tree height-diameter relationships in the central congo basin. *Annals of Forest Science*,
861 **74**, 7.
- 862 Kopecký, M., Macek, M. and Wild, J. (2021) Topographic wetness index calculation guidelines based on measured soil moisture
863 and plant species composition. *Science of the Total Environment*, **757**, 143785.
- 864 Kraft, N. J., Adler, P. B., Godoy, O., James, E. C., Fuller, S. and Levine, J. M. (2015) Community assembly, coexistence and the
865 environmental filtering metaphor. *Functional ecology*, **29**, 592–599.
- 866 Kükenbrink, D., Hueni, A., Schneider, F. D., Damm, A., Gastellu-Etchegorry, J.-P., Schaepman, M. E. and Morsdorf, F. (2019)
867 Mapping the irradiance field of a single tree: Quantifying vegetation-induced adjacency effects. *IEEE Transactions on
868 Geoscience and Remote Sensing*, **57**, 4994–5011.
- 869 Kukkonen, M., Maltamo, M., Korhonen, L. and Packalen, P. (2019) Multispectral airborne lidar data in the prediction of boreal
870 tree species composition. *IEEE Transactions on Geoscience and Remote Sensing*, **57**, 3462–3471.
- 871 Landini, G. (2010) Particles8 class: An imagej plugin for estimating various statistics of binary 8-connected particles. *Tech.
872 rep.* URL: <https://blog.bham.ac.uk/intellimic/g-landini-software>. Accessed on November 25, 2022.
- 873 Li, N., Ho, C. P., Xue, J., Lim, L. W., Chen, G., Fu, Y. H. and Lee, L. Y. T. (2022) A progress review on solid-state lidar and
874 nanophotonics-based lidar sensors. *Laser & Photonics Reviews*, **16**, 2100511.
- 875 Lim, K. S. and Treitz, P. M. (2004) Estimation of above ground forest biomass from airborne discrete return laser scanner data
876 using canopy-based quantile estimators. *Scandinavian Journal of Forest Research*, **19**, 558–570.
- 877 Liu, F. T., Ting, K. M. and Zhou, Z.-H. (2008) Isolation forest. In *2008 eighth ieee international conference on data mining*, 413–
878 422. IEEE.
- 879 Liu, X., Hao, Y., Widagdo, F. R. A., Xie, L., Dong, L. and Li, F. (2021) Predicting height to crown base of larix olgensis in northeast
880 china using uav-lidar data and nonlinear mixed effects models. *Remote Sensing*, **13**, 1834.
- 881 Liu, Y.-F., Jaw, D.-W., Huang, S.-C. and Hwang, J.-N. (2018) Desnownet: Context-aware deep network for snow removal. *IEEE
882 Transactions on Image Processing*, **27**, 3064–3073.
- 883 Lo, C.-S. and Lin, C. (2012) Growth-competition-based stem diameter and volume modeling for tree-level forest inventory
884 using airborne lidar data. *IEEE Transactions on Geoscience and Remote Sensing*, **51**, 2216–2226.
- 885 LTER-Europe (2007) Integrated european long-term ecosystem, critical zone and socio-ecological research. URL: <https://elter-ri.eu/>. Accessed: 2023-02-04.
- 887 Luo, W., Li, Y., Urtasun, R. and Zemel, R. (2016) Understanding the effective receptive field in deep convolutional neural
888 networks. *Advances in neural information processing systems*, **29**.
- 889 Ma, X., Migliavacca, M., Wirth, C., Bohn, F. J., Huth, A., Richter, R. and Mahecha, M. D. (2020) Monitoring plant functional
890 diversity using the reflectance and echo from space. *Remote Sensing*, **12**, 1248.

- 891 Maestre, F. T., Callaway, R. M., Valladares, F. and Lortie, C. J. (2009) Refining the stress-gradient hypothesis for competition
892 and facilitation in plant communities. *Journal of ecology*, **97**, 199–205.
- 893 Marques, O., Barenholtz, E. and Charvillat, V. (2011) Context modeling in computer vision: techniques, implications, and
894 applications. *Multimedia Tools and Applications*, **51**, 303–339.
- 895 Miller, V. C. (1953) A quantitative geomorphic study of drainage basin characteristics in the clinch mountain area of virginia
896 and tennessee, usa. *Tech. rep.*, Columbia Univ New York.
- 897 Mittal, S., Sharma, I., Kumar, A. et al. (2023) Comparative analysis of shallow learning and deep learning. In *2023 International
898 Conference on Next Generation Electronics (NEleX)*, 1–8. IEEE.
- 899 Mohamedou, C., Tokola, T. and Eerikäinen, K. (2017) Lidar-based twi and terrain attributes in improving parametric predictor
900 for tree growth in southeast finland. *International journal of applied earth observation and geoinformation*, **62**, 183–191.
- 901 Muscarella, R., Messier, J., Condit, R., Hubbell, S. P. and Svenning, J.-C. (2018) Effects of biotic interactions on tropical tree
902 performance depend on abiotic conditions. *Ecology*, **99**, 2740–2750.
- 903 Næsset, E. (1997) Determination of mean tree height of forest stands using airborne laser scanner data. *ISPRS Journal of
904 Photogrammetry and Remote sensing*, **52**, 49–56.
- 905 Næsset, E. and Økland, T. (2002) Estimating tree height and tree crown properties using airborne scanning laser in a boreal
906 nature reserve. *Remote Sensing of Environment*, **79**, 105–115.
- 907 Oehmcke, S., Li, L., Revenga, J. C., Nord-Larsen, T., Trepekli, K., Gieseke, F. and Igel, C. (2022) Deep learning based 3d point
908 cloud regression for estimating forest biomass. In *Proceedings of the 30th International Conference on Advances in Geographic
909 Information Systems*, 1–4.
- 910 Pillar, V. D., Duarte, L. d. S., Sosinski, E. E. and Joner, F. (2009) Discriminating trait-convergence and trait-divergence assembly
911 patterns in ecological community gradients. *Journal of Vegetation Science*, **20**, 334–348.
- 912 Pörtner, H.-O., Roberts, D. C., Adams, H., Adler, C., Aldunce, P., Ali, E., Begum, R. A., Betts, R., Kerr, R. B., Biesbroek, R. et al.
913 (2022) *Climate change 2022: Impacts, adaptation and vulnerability*. IPCC Geneva, Switzerland.
- 914 Potvin, C. and Dutilleul, P. (2009) Neighborhood effects and size-asymmetric competition in a tree plantation varying in diver-
915 sity. *Ecology*, **90**, 321–327.
- 916 Quionero-Candela, J., Sugiyama, M., Schwaighofer, A. and Lawrence, N. D. (2009) *Data Set Shift in Machine Learning*. MIT
917 Press, Cambridge, Massachusetts. <http://www.acad.bg/ebook/ml/The.MIT.Press.Dataset.Shift.in.Machine.Learning.Feb.2009.eBook-DDU.pdf>.
- 919 Ratcliffe, S., Holzwarth, F., Nadrowski, K., Levick, S. and Wirth, C. (2015) Tree neighbourhood matters—tree species composi-
920 tion drives diversity–productivity patterns in a near-natural beech forest. *Forest Ecology and Management*, **335**, 225–234.
- 921 Réjou-Méchain, M., Barbier, N., Couteron, P., Ploton, P., Vincent, G., Herold, M., Mermoz, S., Saatchi, S., Chave, J., De Boissieu,
922 F. et al. (2019) Upscaling forest biomass from field to satellite measurements: sources of errors and ways to reduce them. *Surveys in Geophysics*, **40**, 881–911.
- 924 Revenga, J. C., Trepekli, K., Oehmcke, S., Jensen, R., Li, L., Igel, C., Gieseke, F. C. and Friborg, T. (2022) Above-ground biomass
925 prediction for croplands at a sub-meter resolution using uav-lidar and machine learning methods. *Remote Sensing*, **14**,
926 3912.
- 927 Rijal, B., Weiskittel, A. R. and Kershaw Jr, J. A. (2012) Development of height to crown base models for thirteen tree species
928 of the north american acadian region. *The Forestry Chronicle*, **88**, 60–73.
- 929 Rosin, P. L. (1999) Measuring rectangularity. *Machine Vision and Applications*, **11**, 191–196.

- 930 Santini, F., Kefauver, S. C., Resco de Dios, V., Araus, J. L. and Voltas, J. (2019) Using unmanned aerial vehicle-based multispectral, rgb and thermal imagery for phenotyping of forest genetic trials: A case study in *pinus halepensis*. *Annals of Applied Biology*, **174**, 262–276.
- 933 Schapire, R. E. (2013) Explaining adaboost. *Empirical Inference: Festschrift in Honor of Vladimir N. Vapnik*, 37–52.
- 934 Schiefer, F., Kattenborn, T., Frick, A., Frey, J., Schall, P., Koch, B. and Schmidlein, S. (2020) Mapping forest tree species in high resolution uav-based rgb-imagery by means of convolutional neural networks. *ISPRS Journal of Photogrammetry and Remote Sensing*, **170**, 205–215.
- 937 Schumm, S. A. (1956) Evolution of drainage systems and slopes in badlands at perth amboy, new jersey. *Geological society of America bulletin*, **67**, 597–646.
- 939 Scrinzi, G., Galvagni, D. and Marzullo, L. (2010) *I nuovi modelli dendrometrici per la stima delle masse assestamentali in Provincia di Trento*. Provincia autonoma di Trento. Servizio foreste e fauna.
- 941 Steiniger, S. and Blake, L. (2022) Openjump software. *Tech. rep.* URL: www.openjump.org.
- 942 Strahler, A. N. (1952) Hypsometric (area-altitude) analysis of erosional topography. *Geological society of America bulletin*, **63**, 1117–1142.
- 944 Sun, S., Cao, Q. V. and Cao, T. (2019) Evaluation of distance-independent competition indices in predicting tree survival and diameter growth. *Canadian Journal of Forest Research*, **49**, 440–446.
- 946 Swiss FluxNet (1997) Swiss fluxnet: National greenhouse gas flux measurement network. URL: <https://www.swissfluxnet.ethz.ch/>. Accessed: 2023-02-04.
- 948 – (2024) Site history: Ch-dav. URL: <https://www.swissfluxnet.ethz.ch/index.php/sites/site-info-ch-dav/history/>. Accessed: 2026-01-12.
- 950 Tibshirani, R. (1996) Regression shrinkage and selection via the lasso. *Journal of the Royal Statistical Society: Series B (Methodological)*, **58**, 267–288.
- 952 TreeNet (2023) Biological drought and growth indicator network. URL: <https://treenet.info/>. Accessed: 2023-02-04.
- 953 Valladares, F., Arrieta, S., Aranda, I., Lorenzo, D., Sánchez-Gómez, D., Tena, D., Suárez, F. and Pardos, J. A. (2005a) Shade tolerance, photoinhibition sensitivity and phenotypic plasticity of *ilex aquifolium* in continental mediterranean sites. *Tree physiology*, **25**, 1041–1052.
- 956 Valladares, F., Dobarro, I., Sánchez-Gómez, D. and Pearcy, R. W. (2005b) Photoinhibition and drought in mediterranean woody saplings: scaling effects and interactions in sun and shade phenotypes. *Journal of Experimental Botany*, **56**, 483–494.
- 958 Valladares, F., Gianoli, E. and Gómez, J. M. (2007) Ecological limits to plant phenotypic plasticity. *New phytologist*, **176**, 749–763.
- 960 Valladares, F. and Niinemets, Ü. (2008) Shade tolerance, a key plant feature of complex nature and consequences. *Annual Review of Ecology, Evolution, and Systematics*, **39**, 237–257.
- 962 Vidaurre, D., Bielza, C. and Larranaga, P. (2013) A survey of l1 regression. *International Statistical Review*, **81**, 361–387.
- 963 Wadell, H. (1935) Volume, shape, and roundness of quartz particles. *The Journal of Geology*, **43**, 250–280.
- 964 Wang, C.-J., Zhang, Z.-X. and Wan, J.-Z. (2019) Vulnerability of global forest ecoregions to future climate change. *Global Ecology and Conservation*, **20**, e00760.
- 966 Westerholt, R., Resch, B., Mocnik, F.-B. and Hoffmeister, D. (2018) A statistical test on the local effects of spatially structured variance. *International Journal of Geographical Information Science*, **32**, 571–600.

- 968 Wilcoxon, F. (1992) *Individual comparisons by ranking methods*. Springer.
- 969 WSL (1985) Methods of the sanasilva inventory. *Tech. rep.*, Swiss Federal Institute for Forest, Snow and Landscape Re-
970 search (WSL). URL: <https://www.wsl.ch/en/forest/forest-development-and-monitoring/sanasilva-forest-health-inventory/>. Accessed: 2023-02-04.
- 971
- 972 – (1994) Long-term forest ecosystem research (lwf). URL: <https://lwf.wsl.ch/en/>. Accessed: 2023-02-04.
- 973 Xu, D., Wang, H., Xu, W., Luan, Z. and Xu, X. (2021) Lidar applications to estimate forest biomass at individual tree scale:
974 Opportunities, challenges and future perspectives. *Forests*, **12**, 550.
- 975 Yang, W., Tan, R. T., Feng, J., Liu, J., Guo, Z. and Yan, S. (2017) Deep joint rain detection and removal from a single image. In
976 *Proceedings of the IEEE conference on computer vision and pattern recognition*, 1357–1366.
- 977 Yang, Z., Liu, Q., Luo, P., Ye, Q., Sharma, R. P., Duan, G., Zhang, H. and Fu, L. (2020) Nonlinear mixed-effects height to crown
978 base model based on both airborne lidar and field datasets for picea crassifolia kom trees in northwest china. *Forest Ecology
and Management*, **474**, 118323.
- 979
- 980 Yao, W., Krull, J., Krzystek, P. and Heurich, M. (2014) Sensitivity analysis of 3d individual tree detection from lidar point clouds
981 of temperate forests. *Forests*, **5**, 1122–1142.
- 982 Zăvoianu, I. (1978) *Morfometria bazinelor hidrografice*. Editura Academiei Republicii Socialiste România.
- 983 Zhang, B., Sajjad, S., Chen, K., Zhou, L., Zhang, Y., Yong, K. K. and Sun, Y. (2020) Predicting tree height-diameter relation-
984 ship from relative competition levels using quantile regression models for chinese fir (*cunninghamia lanceolata*) in fujian
985 province, china. *Forests*, **11**, 183.
- 986 Zhao, R., Ouyang, W., Li, H. and Wang, X. (2015) Saliency detection by multi-context deep learning. In *Proceedings of the IEEE
Conference on Computer Vision and Pattern Recognition (CVPR)*, 1265–1274.
- 987
- 988 Zheng, Z., Zeng, Y., Schuman, M. C., Jiang, H., Schmid, B., Schaepman, M. E. and Morsdorf, F. (2022) Individual tree-based vs
989 pixel-based approaches to mapping forest functional traits and diversity by remote sensing. *International Journal of Applied
Earth Observation and Geoinformation*, **114**, 103074.
- 990
- 991 Zingg, T. (1935) *Beitrag zur schotteranalyse*. Ph.D. thesis, ETH Zurich.
- 992 Zunic, J. and Rosin, P. L. (2004) A new convexity measure for polygons. *IEEE Transactions on Pattern Analysis and Machine
Intelligence*, **26**, 923–934.
- 993